Iowa State University
Digital Repository

Graduate Theses and Dissertations | Iowa State University Capstones, Theses and Dissertations

2010

Machining induced defects in Relaxor ferroelectric PMN-PT crystals

Cheng Deng
Iowa State University

Follow this and additional works at: https://lib.dr.iastate.edu/etd

Part of the Aerospace Engineering Commons

Recommended Citation
Deng, Cheng, "Machining induced defects in Relaxor ferroelectric PMN-PT crystals" (2010). *Graduate Theses and Dissertations*. 11784.
https://lib.dr.iastate.edu/etd/11784

This Thesis is brought to you for free and open access by the Iowa State University Capstones, Theses and Dissertations at Iowa State University Digital Repository. It has been accepted for inclusion in Graduate Theses and Dissertations by an authorized administrator of Iowa State University Digital Repository. For more information, please contact digirep@iastate.edu.

Machining induced defects in Relaxor ferroelectric PMN-PT crystals

by

Cheng Deng

A thesis submitted to the graduate faculty

in partial fulfillment of the requirements for the degree of

MASTER OF SCIENCE

Major: Engineering Mechanics

Program of Study Committee:
Ashraf F. Bastawros, Major Professor
Thomas J. Rudolphi
Wei Hong

Iowa State University

Ames, Iowa

2010

TABLE OF CONTENTS

LIST OF FIGURES iii

LIST OF TABLES iv

ABSTRACT v

CHAPTER 1. INTRODUCTION AND LITERATURE REVIEW 1
- 1.1 Literature Review on Wire Saw and PMN-PT Single Crystals 4
  - 1.1.1 Basic Mechanisms and Material Removal Models of Wire Saw 4
  - 1.1.2 PMN-PT Single Crystals 8
- 1.2 Typical Damages Induced By Wire Saw Process 10
- 1.3 Motivation and Proposed Work 10
- 1.4 Thesis Organization 14

CHAPTER 2. EXPERIMENTAL PROCEDURE 15
- 2.1 Wire Saw Process, Wire Speed, and Feed Speed Measurements 15
- 2.2 Wire Bow Angle Measurements 17
- 2.3 Diamond Grit-Coated Steel Wires and Abrasive Slurry 18
- 2.4 Vibration Assistance Setup 19
- 2.5 Preliminary Results 21
  - 2.5.1 Roughness Evolution 21
  - 2.5.2 Waviness Evolution 31

CHAPTER 3. PHASE TRANSFORMATION ANALYSIS 39
- 3.1 Introduction 39
- 3.2 Experimental Methods 42
- 3.3 Results and Discussion 43
  - 3.3.1 X-ray results 43
  - 3.3.2 Raman Scattering Results 47
- 3.4 Conclusion 50

CHAPTER 4 SUMMARY AND DISCUSSION 51

BIBLIOGRAPHY 52

ACKNOWLEDGEMENTS 56

LIST OF FIGURES

Figure 1.1 Schematic diagram of the principle of the ID Saw technique 2
Figure 1.2 Schematic diagram of the “rolling-indenting” process in wire saw manufacturing process under Free Abrasive Machining 3
Figure 1.3 Schematic diagram shows the principle of the multi-wire sawing technique 4
Figure 1.4 Free abrasive wire saw process 7
Figure 1.5 Surfaces of wire saw sliced wafer 8
Figure 1.6 ABO_3 perovskite structure 10
Figure 1.7 Phase diagram of PMN-PT 10
Figure 1.8 Optical image shows the surface waviness, roughness, chipping 11
Figure 1.9 3D surface reconstruction shows wire saw induced roughness as measured by surface profilometer 11
Figure 1.10 3D surface reconstruction shows wire saw induced waviness as measured by surface profilometer 12
Figure 1.11 SEM image of a cut sample subsurface cracks 12
Figure 2.1 Single wire, spool-to-spool wire saw machine (DWT Inc., Millennium Model) used in wire saw tests 16
Figure 2.2 Optical image shows the wire inclination angle with the cutting direction at the entrance and exit from the specimen 17
Figure 2.3 Wire bow angle and wire curvature 18
Figure 2.4 Schematic diagram shows the shielding effect 20
Figure 2.5 Optical image shows the vibration-assisted cutting process 20
Figure 2.6 The variation of surface roughness Ra and RMS as a function of V_x 24
Figure 2.7 3D surface reconstruction images show wire saw cut surfaces roughness as measured by Zygo profilometer 29
Figure 2.8 SEM images of wire saw cut surfaces 31
Figure 2.9 The variation of surface waviness Ra and RMS as a function of V_x 33
Figure 2.10 3D surface reconstruction images show wire saw cut surfaces waviness as measured by Zygo profilometer 38
Figure 3.1 Phase transformations between the rhombohedral and orthorhombic phases induced by stress 40
Figure 3.2 The stress induced depolarization in the presence of a small bias electric field 41
Figure 3.3 X-ray diffraction pattern of <0 0 1> oriented PMN-0.30PT single crystals cut by wire saw, ID saw and theoretical 45
Figure 3.4 Selected regions of the X-ray diffraction pattern of <0 0 1> oriented PMN-0.30PT single crystals cut by wire saw, ID saw and theoretical 47
Figure 3.5 Raman spectra of the <0 0 1> oriented PMN-0.30PT single crystal wafer at different locations that parallel and perpendicular to the waviness direction 49
Figure 3.6 Selected region of Raman spectra of the <0 0 1> oriented PMN-0.30PT single crystal wafer at different locations that perpendicular to the waviness direction 49
Figure 3.7 Selected region of Raman spectra of the <0 0 1> oriented PMN-0.30PT single crystal wafer at different locations that parallel to the waviness direction 50

LIST OF TABLES

Table 2.1. Diamond impregnated wire properties 19

ABSTRACT

The superior piezoelectric and dielectric properties of the relaxor based piezoelectric single crystals (PMN-PT) render them as prime candidates for Navy sonar detectors as well as in broad band medical ultrasonic imaging devices. Production of phased array probes utilizing these types of high performance ceramics requires dicing these crystals to arrays with pitches of less than the desired wavelength, ranging from tens to hundreds of micrometers. However, the relaxor based single crystals are very brittle with fracture toughness of about a third to a half that of typical PZT ceramics ($0.4 - 0.8 MPa\sqrt{m}$). Excessive chipping and cracking, either during the cutting or poling process, have been reported as major hurdles in processing, leading to spurious resonance and degradation of the distance resolution. In addition, residual stress from the cutting process could be major reliability degradation if it is not well quantified and minimized.

In this work, we experimentally analyzed the machining induced damage in a group of Lead Magnesium Niobate-Lead Titanate solid solution single crystal {(1-x)[$Pb(Mg_{1/3}Nb_{2/3})O_3$]-x[$PbTiO_3$] (PMN-PT)} under simulated process parameters for cutting speeds and down feeds. The machined surfaces are examined by non-contact optical profilometer for planarity and roughness, scanning electron microscopy for subsurface damage, and by micro-raman spectroscopic analysis and X-ray diffraction analysis to uncover machining induced phase transformations. The analysis reveals the preferred process parameters for minimal machining induced damages.

CHAPTER 1. INTRODUCTION AND LITERATURE REVIEW

The single crystals wafers of lead magnesium niobate-lead titanate solid solution, (1-x)[Pb($Mg_{1/3}Nb_{2/3}$)O_3]-x[$PbTiO_3$] (PMN-PT) are very attractive for sonar and ultrasonic detectors applications because of their high piezoelectric coefficients and good electromechanical coupling. Correspondingly, high yield wafer manufacturing to produce large PMN-PT wafers with controlled surface roughness and small kerf loss is essential. In this work, the quality of a wire saw cut surface of these crystals are studied experimentally to show the limits on surface roughness and subsurface damage.

The traditional manufacturing process to produce wafers with controlled surface roughness utilizes an inner diameter (ID) saw [1-3] in the slicing single crystalline ingot, followed by various grinding, polishing, and cleaning processes. The principle of ID saw is shown in Fig.1.1. It is made of a stack of thin annular ring blades. The inner perimeter is coated with micro-size diamond grits. The outer perimeter of the blade is stretched under high tension. The ingot is fed through the center, while the blade traverses through the ingot, and then a slice of wafer is produced. The process of material removal is a "ploughing" process. An ID saw is a fast slicing process, thought it suffers from large kerf loss (typically 350 μm for silicon wafers) and excessive surface roughness and subsurface damage. [1] To avoid large kerf loss and increase the wafer surface quality, wire saw-based cutting technology [1, 4-7] was developed and gained widespread utilization in the slicing of silicon and piezoelectric ceramic wafers. Compared with an ID saw, a wire saw exhibits many advantages, such as higher throughput, less wafer-surface damage, lower kerfs loss and almost no restrictions on the size of the ingots. [8]

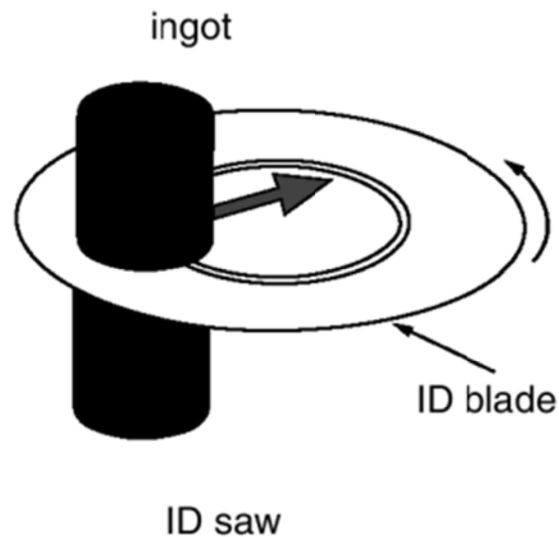

Fig. 1.1 Schematic diagram of the principle of the ID Saw technique

In modern wire saw manufacturing processes, a bar steel wire (typically around 175μm in diameter) is stretched with high tension (typically 20–35 N), runs at cutting speed of V_x =1-10 m/s and is fed to cut the bowel at a feed rate of V_z =1-10 μm/s [1,9]. Two types of cutting systems are used; free abrasive (an abrasive based slurry with bare wire), or fixed abrasive (brazed abrasive to the wire). In free abrasive machining (FAM) process, the abrasive particles, such as silicon carbide, or diamond, are constrained to roll and indent the cutting zone between the wire and the substrate as seen in Fig.1.2. Through the ''rolling-indenting'' process the abrasives are squeezed and sheared between the wire and the work piece. As a result, they penetrate, roll, indent, and scratch the surface to generate web of cracks and remove material from the work piece [9,10]. Wafer thicknesses are around 250 and 350 μm and above. A thickness of 100 μm can be also obtained. The slurry can be water-based or oil-based. Oil-based slurry causes the wafers to stick to each other, and it is hard to separate them, while removal of the oil from the wafer surface is another problem. Disposal of the oil-based slurry after use is also a problem. Hydrogen gas is produced due to

interaction of water-based slurry and silicon, which may cause an explosion. However, from an environmental point of view, considering the high amount of slurry disposed during the process, water-based slurries can be a choice for the future of the wire saw process [8].

For multi-wire saw technology, its principle is depicted in Fig. 1.3. A single wire is fed from a supply spool through a pulley and tension control unit to the four wire guides that are grooved with a constant pitch. Multiple strands of a wire net (known as a web) are formed by winding the wire on the wire guides through parallel grooves. Which may be as high as 700. A take-up spool collects the used wire. The wire is pulled by the torque exerted by the main drive and slave as shown. The tension on the wire is maintained by the feedback control unit at a prescribed value. The single column on the holder is pushed against the moving wire web and sliced into hundreds of wafers at the same time. The wire either moves in one direction or oscillates back and forth with a 90-95% overlap, so that each a uniform kerf can be maintained throughout the cutting process. The wire material is usually stainless steel. To increase the productivity and to be able to cut harder ceramics, diamond impregnated wire, which leads to fixed abrasive machining, was developed [11,12].

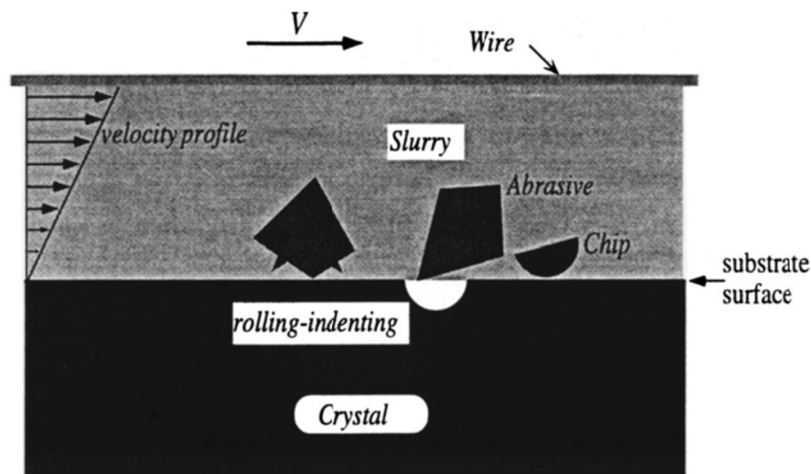

Fig. 1.2 Schematic diagram of the “rolling-indenting” process in wire saw manufacturing process under Free Abrasive Machining (FAM). (Fuqian and Kao, 2001).

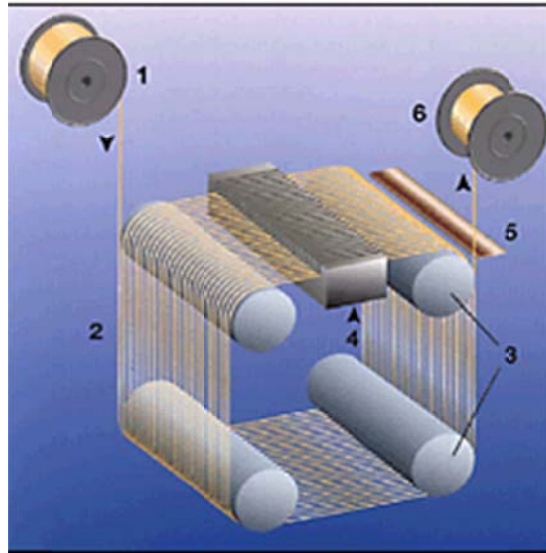

Fig.1.3 Schematic diagram shows the principle of the multi-wire sawing technique. The crystal (work piece) is pushed against the wire web with a constant feeding rate which is equal to the sawing rate. (Moller H. J. 2004)

1.1 Literature Review on Wire Saw & PMN-PT Single Crystals

The basic material removal mechanisms and several models of the wire saw process are reviewed. The main materials related characteristics are also presented for the studied PMN-PT single crystals with different composition.

1.1.1 Basic Mechanisms and Material Removal Models of Wire Saw

Free abrasive cutting process is derived by Moller [8], utilizing fracture mechanics and hydrodynamic behavior of slurry. The interaction between the wire, abrasive grit, and work pieces are considered in semi-contact or non-contact mode. A semi-contact is established if the hydrodynamic slurry film thickness between the wire and work piece is smaller than the average abrasive grit size, and thereby a three body contact is established between the abrasive grit, the wire and work piece. In the non-contact mode, the grit is rolling freely between the wire and work piece and can remain in contact with either the wire

or work piece. The material removal rate (MRR) for semi-contact and non-contact cases is developed. If the elastic displacement of the wire is significant and slurry viscosity changes are negligible, this regime is defined as isoviscous-elastic regime (IE). If the slurry film thickness is much more than the elastic displacement of the wire, it is called isoviscous-rigid regime (IR). The slurry film thickness and shear stress are defined for both regimes. The increase of abrasive grit size increases the material removal rate (MRR) while also increasing surface roughness of the final product.

The abrasive grit shape is also important in wire saw MRR. If the abrasive grit has a high aspect ratio (elongated grit), it will not rotate in the laminar flow of slurry, which will decrease MRR, while grits having an aspect ratio close to one will rotate more easily and increase the MRR. Accordingly, freshly applied slurry will have grits with sharp corners that will increase the MRR. The increase of viscosity of the slurry due to debris from the work piece may cause agglomeration and reduce MRR. The wire saw process induces a wavy topology with mm scale wavelength, and local roughness in the micro and sub-micron range. The origin of such large-scale defects, grooves and wavy topologies are not yet well understood.

Bhagavat et al. [10] defined the material removal rate as a function of the imparted energy to the abrasive by hydrodynamic forces. The hydrodynamic film characteristics are calculated using the finite element method, which couples Reynolds' equation of hydrodynamics with the elasticity equation of wire. Such an analysis provides the pressure distribution and film thickness profiles of slurry film within the cut trench. Across the ingot diameter, the pressure starts from zero at the inlet and gradually increases to a maximum value, where it starts to decrease towards the downstream exit region as seen in Fig. 1.4(a).

The gradual decrease of pressure near the exit is disturbed by a stage in the pressure profile that is due to the continuity of slurry flow. The pressure profile is almost constant in the transverse direction except near the entrance and exits where it decays to zero. The thickness profile of the slurry film shows that the film thickness is large at the inlet, where it starts to decrease gradually towards the exit as seen in Fig. 1.4(b). The high slurry film thickness at the inlet is due to high wire compliance at the inlet, while the low slurry film thickness at the middle is explained by the low wire compliance in this region. The minimum slurry film thickness at the exit is explained by the low slurry pressure. The increase of slurry viscosity and wire speed V_x increases the slurry film thickness, while the increase of the wire bow angle decreases the film thickness due to an increase in stiffness of the wire and load on the film. The obtained minimum film thickness for a 50 mm ingot was approximately 130 μm, which is much greater than abrasive grit size. Thus, the mode of cutting is free abrasive machining in which the grits roll and indent the work piece to induce material removal. This is also validated by the microscopic images of a wire saw sliced wafer which has equal-sized pits due to single material removal of floating abrasives as in Fig. 1.5(a). The polished surface of a wafer shows scratches due to direct contact of abrasive pressed by the tool onto ingot as presented in Fig. 1.5(b). Due to the decrease of slurry film thickness towards the exit, the cutting conditions may change for large diameter ingots and poor surface finish occurs. Oscillating wire saw machining is necessary for uniform and efficient cutting of large diameter ingots. The wire saw machining is taking place in an isoviscous-elastic regime (IE). The material removal is proportional to slurry viscosity μ, size of abrasive D_g, slurry pressure P_s, square of wire speed V_x, and inversely proportional to square of slurry thickness h_s as presented in Eq. 1.1[10, 13].

$$MRR \approx \mu D_g p_s (\frac{V_x}{h_s})^2 \quad (1.1)$$

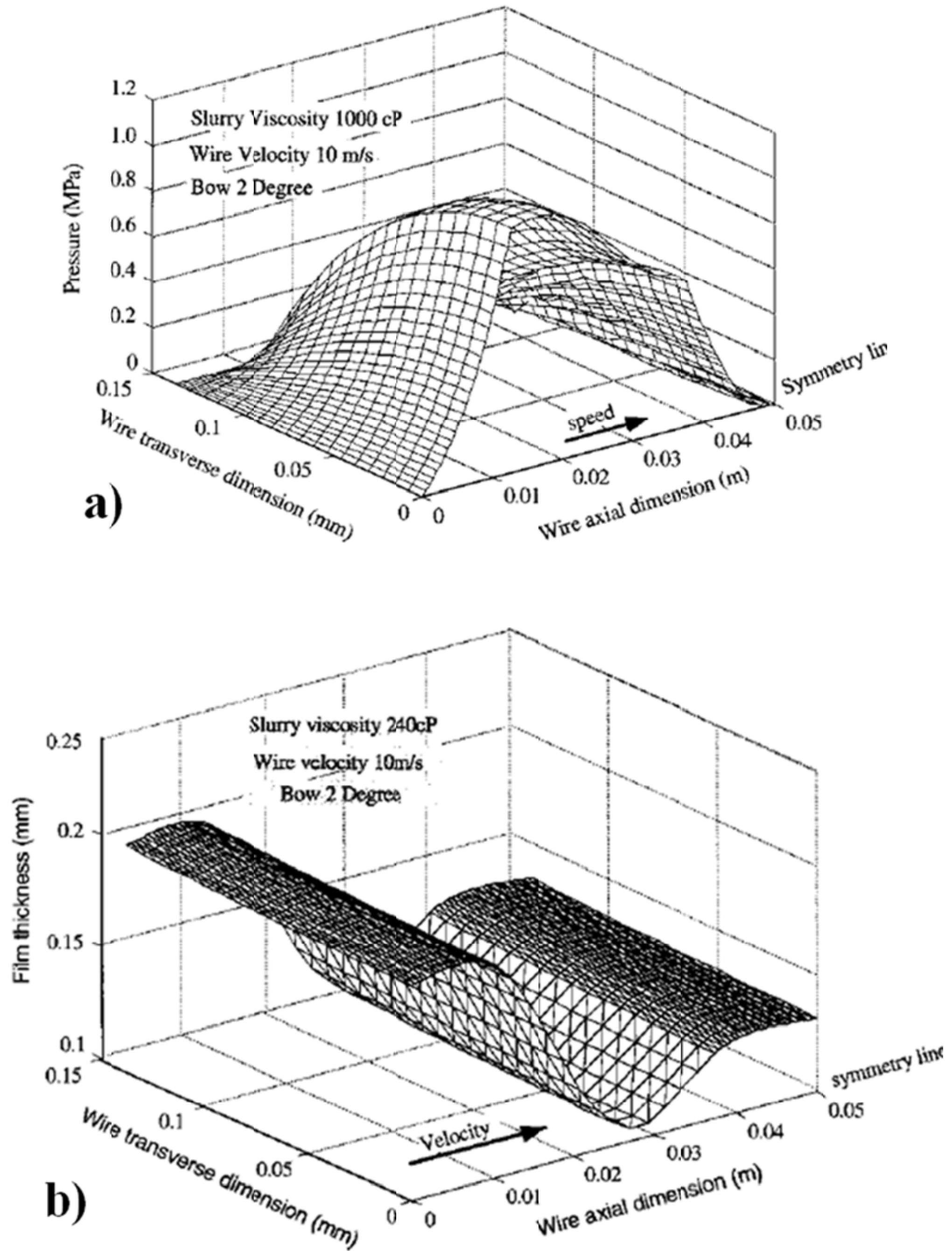

Fig.1.4. Free abrasive wire saw process a) The slurry pressure profile b) Slurry film thickness profile (Bhagavat et al. 2000).

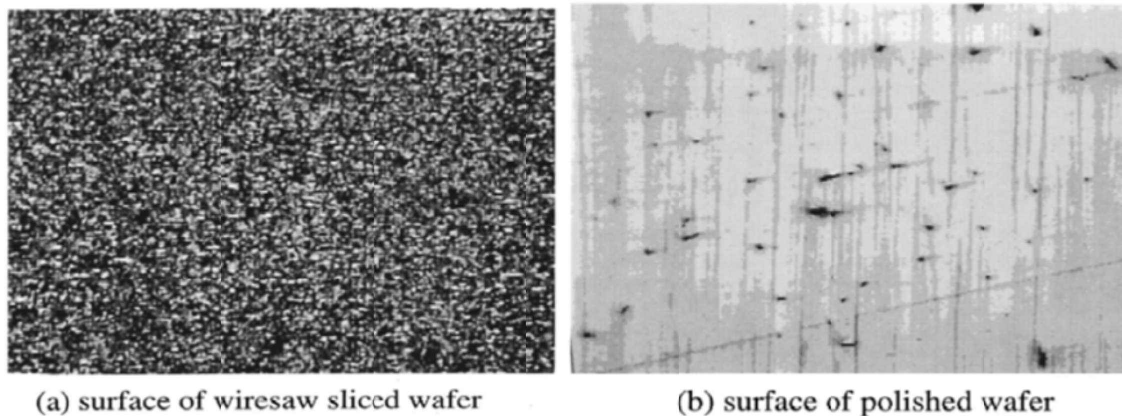

Fig.1.5. Surfaces of a) Wire saw sliced wafer with free abrasive machining b) Polished wafer (Bhagavat et al. 2000).

1.1.2 PMN-PT Single Crystals

The single crystals of lead magnesium niobate-lead titanate solid solution, (1-x)[$Pb(Mg_{1/3}Nb_{2/3})O_3$]-x[$PbTiO_3$] (PMN-PT) are a new generation of piezoelectric materials. The piezoelectric effect is associated with a lack of charge symmetry about the center of a unit cell [14]. The separation of the positive and negative charge centers in a unit cell is directly related to the spontaneous strain and electric displacement. Change in the equilibrium distance between charge centers is called the linear piezoelectric effect. The new material of PMN- x PT single crystals was formulated to exhibit very large electromechanical coupling coefficients, high piezoelectric coefficients, high dielectric constants and low dielectric losses that results in improving bandwidth, sensitivity and source level. Therefore, it is widely used as important devices in medicine, telecommunications, as well as in high technology and military industries. Like the other ceramics, single crystals of PMN-PT are very brittle.

The PMN-PT solid solutions belong to the family of perovskite structure materials with the general formula ABO_3 can be seen in Fig. 1.6. The sub-lattice A is occupied by Pb^{2+}

ions, while the B site is occupied by randomly distributed Mg^{2+}, Nb^{5+}, and Ti^{4+} ions. Recent x-ray diffraction studies have shown that PMN- x PT single crystals at room temperature have a rhombohedral phase structure (Region I) when $x < 0.3$, from which the solid solutions exhibit a relaxor behavior and structural phase transition is from the cubic (P*m3m*) to the rhombohedral (R*3m*) symmetry, and a tetragonal phase (Region Ш) when $x > 0.35$ to 0.37 [15,16], from which the solid solutions show a typical ferroelectric behavior and undergo structural phase transition from the cubic (P*m3m*) to the tetragonal (P*4mm*). The region (Region П) which separates the rhombohedral and tetragonal phase is called the morphotropic phase boundary (MPB), is most commonly investigated since the crystals from this region exhibit the so-called giant piezoelectricity. In this region, the typical relaxor properties vanish and, thus, the solid solutions already tend to exhibit a ferroelectric behavior, and two structural phase transitions are observed, the first is from the cubic (P*m3m*) to the tetragonal (P*4mm*), while the second is from the tetragonal (P*4mm*) to the monoclinic (P*m*) one. However, the problem of symmetry in the MPB region seems to be more complex since the monoclinic symmetry can coexist with a secondary minority rhombohedral or tetragonal phase. Moreover, even the presence of a third minority orthorhombic phase cannot be ruled out. Studies have shown that PMN- x PT specimens near the MPB are in a multiphase state and have speculated that this may be the cause of increased electromechanical properties [15, 17, 18]. The phase diagram has been shown in Fig.1.7. In PMN- x PT single crystals, the spontaneous polarization direction can be switched to another energetically equivalent direction through externally applied loads. In addition of reorienting the polarization, the application of external fields can also initiate phase transformations in relaxor PMN-PT ($0 \leq x \leq 0.33$).

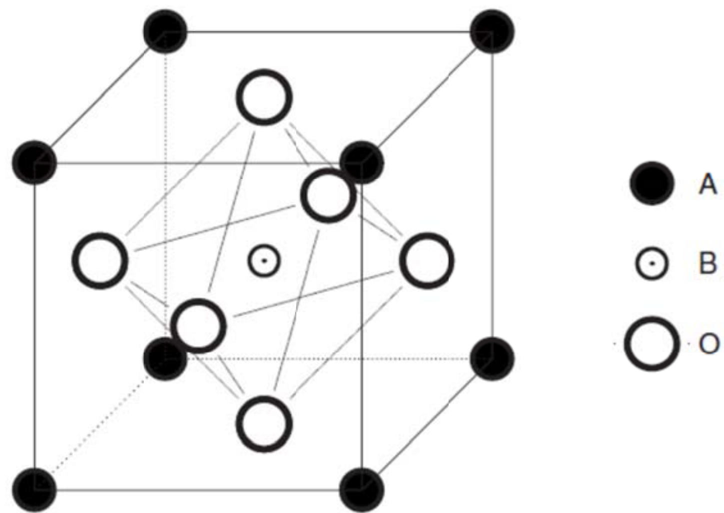

Fig. 1.6 ABO_3 perovskite structure (Noheda, B. et al. 2002)

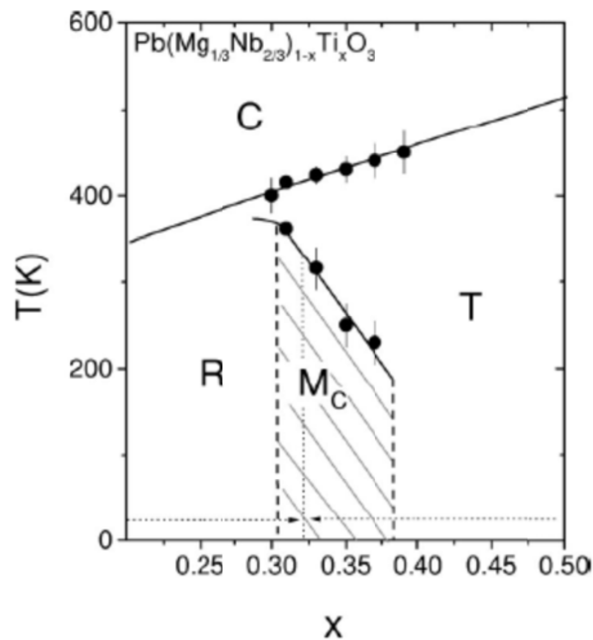

Fig. 1.7 Phase diagram of PMN-PT (Noheda, B. et al. 2002)

1.2 Typical Damages Induced By Wire Saw Process

The wire saw process may induce several surface and subsurface defects of the final PMN- x PT single crystals wafers. These include surface waviness, roughness, chipping and subsurface cracks as seen in Fig.1.8, 1.9, 1.10, 1.11.

The long waviness is induced by the wire drifting in the plane that perpendicular to the cutting down plane, to minimize the total system energy (stored elastic strain energy vs. the work done to cut the crystal). The oblique cutting forces drifts the wire out of the cutting down plane to minimize the cutting energy. This is happening at the expense of increased stored elastic strain energy in the wire. The competition between these two mechanisms induces the long surface waviness. Surface roughness due to chipping and cracking arises from the indentation process of the abrasive grits and the residual stresses they impart on the brittle surface. These contact stresses may also initiate irreversible phase transition with additional residual stresses.

Fig. 1.8 Optical image shows the surface waviness, roughness, chipping

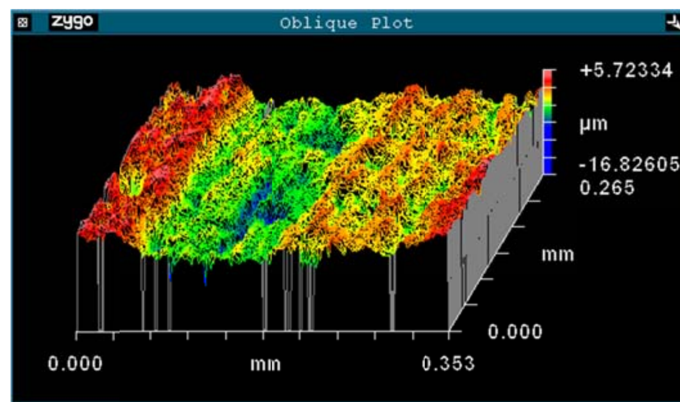

Fig. 1.9 3D surface reconstruction shows wire saw induced roughness as measured by surface profilometer

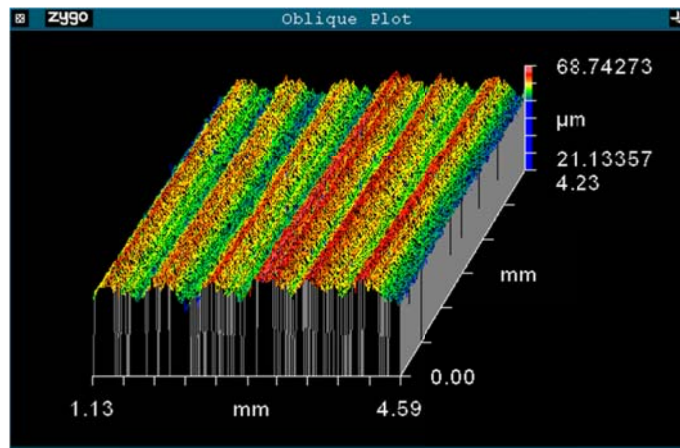

Fig. 1.10 3D surface reconstruction shows wire saw induced waviness as measured by surface profilometer

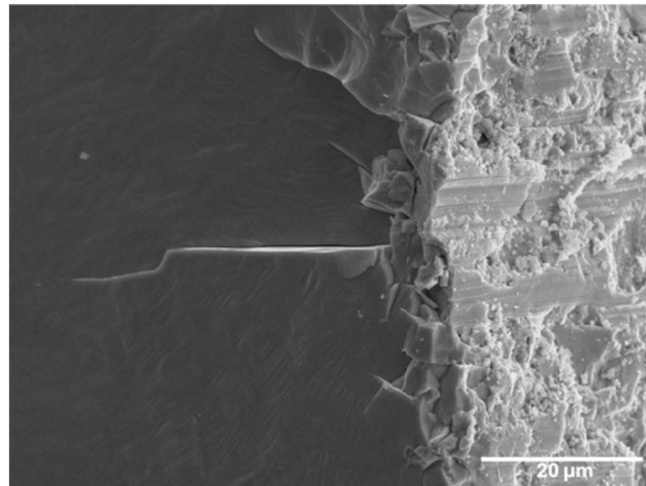

Fig. 1.11 SEM image of a cut sample subsurface cracks

1.3 Motivation and Proposed Work

The single crystal wafers of lead magnesium niobate-lead titanate solid solution, (1-x)[Pb(Mg1/3Nb2/3)O3]-x[PbTiO3](PMN-PT) have large potential applications in transducer applications for sonar and ultrasonic detectors. Wafers with high quality surface characteristics can be obtained by using the wire saw process or the inner diameter (ID) saw. The wire saw process is advantageous over the ID saw because the wire-saw process has a

higher yield, lower kerf loss, and lower surface damage. The wire saw process can be used to cut all kinds of brittle materials with low surface damage and higher yield.

In free abrasive based wire saw, rolling and indenting of the abrasive against the work piece generates material removal. The bow and tension of the wire transfers a hydrodynamic pressure on the abrasive grits through the slurry. The velocity profile of the slurry trapped between the wire and sample, occurring due to wire speed, is providing the motion of the abrasive grits. The combination of hydrodynamic pressure and the motion of the grits results in rolling-indenting motion of grits, which causes material removal in free-abrasive machining. The increase of wire bow or tension may cause disruptions in the hydrodynamic film, which leads to bare wire-sample direct contact. This direct contact creates scratches on the sample, while causing wire breakage. In order to keep the hydrodynamic film, the wire velocity in the abrasive-carrying wire-saw process is high.

Diamond-grit coated steel in the wire-saw process was developed due to the disadvantages of the abrasive-slurry wire-saw process. The diamond-grit coated wire-saw process leads to fixed abrasive machining. This process has a higher yield and less wire breakage in comparison to the abrasive-carrying slurry wire-saw process. In this work, the abrasive-grit coated wire-saw process is investigated.

The wire saw process induces roughness, long waviness and chipping damage on the cut surface, as well as subsurface cracks and possible phase transformation, further possibly a residually stressed region arises. These damages decrease the quality of the wafers and have to be removed by post processes including grinding, lapping, and polishing. However, these post processes increase wafer manufacturing costs.

Subsurface damage could be reduced by vibration-assisted cutting, because intermittent unloading can produce a lateral crack before the median crack fully develops, and upon reloading, the lateral crack shields against further median crack penetration. Furthermore, intermittent unloading produces shielding even for oblique indentation events and intermediate locations of lateral cracks.

The overall goal of this study is to understand the surface roughness and long waviness damage under the abrasive wire cutting and to establish the role of the process parameters. Also, vibration-assisted cutting was set to decrease the subsurface damages; phase transformation was studied and analyzed by Raman Spectra and X-ray diffraction.

1.4 Thesis Organization

The remainder of the dissertation is divided into three chapters. In chapter two, the whole experimental procedure is introduced, after wire saw cutting process, the wafer surfaces' roughness and waviness evolution are studied. In chapter three, investigation of the phase transition is analyzed. In the last chapter, summary of the study is presented.

CHAPTER 2. EXPERIMENTAL PROCEDURE

Wire saw experiments are conducted on PMN-PT single crystal piezoelectrical ceramics. The dynamic cutting forces, wire curvature, wire axial speed, V_x , and feed rate, V_z , are measured during the wire saw cutting tests. The cutting-induced surface roughness and waviness are analyzed for each combination of process parameters with ultrasonic vibration assistance or not. Detailed scanning electron microscope (SEM) analyses are carried out to understand the variation of the machining-induced surface and sub-surface damage with the process parameters. Details of the experimental setup and the corresponding measurements for the range of the investigated process parameters are presented in this chapter.

2.1 Wire Saw Process, Wire Speed, and Feed Speed Measurements

A single spool to spool the wire-saw machine is used in the experiments. The wire is advanced in one direction and then reversed back to 95% of its length, and this allows a 5% refresh rate of the wire per each reversal cycle. The process parameters that can be controlled are the wire-rocking angle, the wire speed, V_x , down feed speed, V_z , wire tension, *T*, and the length of wire used in one reversal of wire, L_w . The tension is controlled by wire tension pulleys powered by air pressure while the rocking motion is controlled by wire guide pulleys as can be seen in Fig. 2.1.

In all experiments, the following parameters have been held constant. A fixed wire length/cut cycle of 300 ft is utilized. Thus, in every forward advance of the wire, a length of $L_w = 300 ft$ (91.4 m) is transferred from one spool to the other. A water-based coolant (Sawzit) at a ratio of 50:1 is used during cutting.

The wire axial speed is a function of spool diameter as the machine controls the speed via the angular speed of the spool. The average wire speed is calibrated via the rotational speed of the guide pulley. The rotational speed is measured by a stroboscope (model Strobex 236)

For every test, twenty stroboscope measurements of the wire guide-pulley rotational speed are acquired in $rev/\min$. The average of these measurements is multiplied by a conversion factor to obtain the speed in meters per second (m/s) as presented in Eq. 2.1. The factor in Eq. 2.1 is obtained using the diameter of the guide pulley.

$$V_x(m/s) = 0.0053 \times (rev/\min) \quad (2.1)$$

The down-feed rate V_z is calibrated by tracking the position of the machine yoke relative to a stationary reference on the machine frame. As the yoke goes down, the relative position changes. The time for the yoke to travel 5 mm is measured during each test.

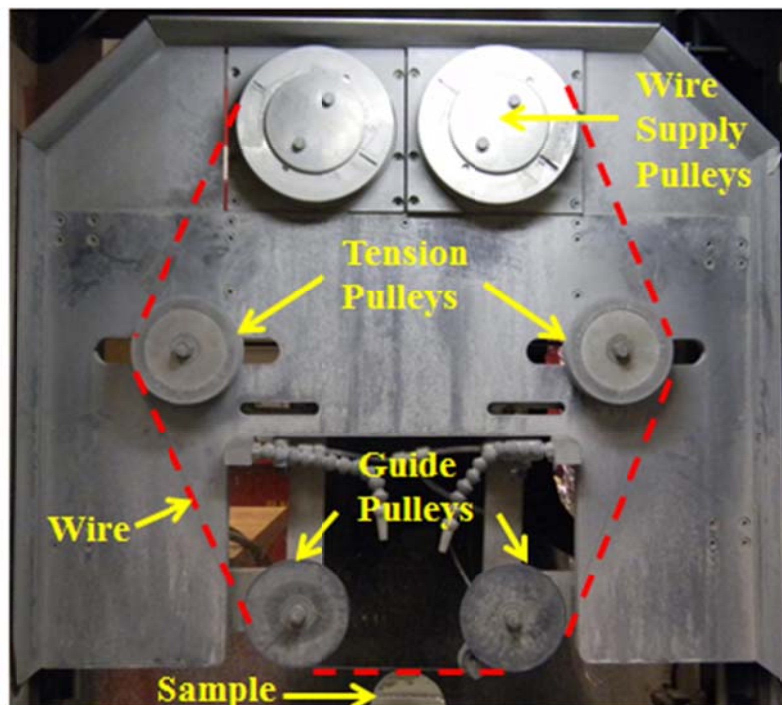

Fig. 2.1 Single wire, spool-to-spool wire saw machine (DWT Inc., Millennium Model) used in wire saw tests. The wire is marked by the dashed line

2.2. Wire Bow Angle Measurements

A megapixel digital camera (Kodak Easy Share DX 7630) of 2856 × 2142 pixels is used to measure the wire bow angle. The images of the wire and sample are collected during the test and analyzed using the Matlab image-processing toolbox to obtain the wire bow angle, α, between the wire and the effective cutting direction. A typical image obtained during a test is presented in Fig. 2.2, for the analysis of α. The slope is at the inlet and exit of the wire; α_1 and α_2 are obtained. For the effective wire bow angle, α is their average. A total of 10 to 15 images are collected in each test, after attaining a steady state wire bow. The average of these measurements represents an average value for α for such test conditions. The wire bow angle α reaches its steady state value after a certain depth of cut and stays constant for the rest of the cut if all of the cutting parameters, including cut length, are constant. Fig. 2.3 shows a sketch of the wire inclination angles and their correlations to the wire curvature.

Fig. 2.2 Optical image shows the wire inclination angle with the cutting direction at the entrance and exit from the specimen

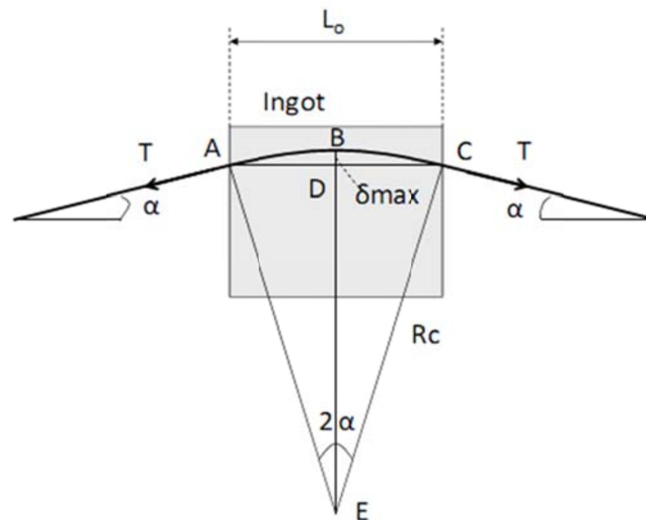

Fig. 2.3 Wire bow angle and wire curvature

2.3. Diamond Grit-Coated Steel Wires and Abrasive Slurry

Two different diamond-grit-coated steel wires and one bare wire then coated with aluminum oxide slurry are used in this study. The wire diameter, D_w, grit size, D_g ,and grit spacing, L_g, of the diamond-grit-coated steel wires are listed in Table 2.1.

Diamond-grit-coated steel wire DWS3 is a product of Well Diamond Wire Saws Inc. The DWS3 has an average diameter of $D_w = 304\mu m$. The average abrasive diamond size is $D_g = 78\mu m$. The average spacing of abrasive grits is $L_g = 280\mu m$. The DWS3 is manufactured by mechanically impregnating the diamonds into the wire. The impregnation process might be successful for some grits, while others just leave an indentation mark on the wire and could not be affixed

Diamond-grit-coated steel wires DWS5 is a product of Saint-Gobain Abrasives Inc, manufactured by nickel electroplating on steel. The grits are affixed into the electroplated nickel layer while the core remains intact. The DWS5 has average diameters of $D_w = 252\mu m$;

average grit sizes of $D_g = 27\mu m$; and average grit spacing of $L_g = 69\mu m$. The grit spacing of DWS5 is very narrow.

Table 2.1. Diamond impregnated wire properties.

Wire name	Diameter D_w(μm)	STD D_w(μm)	Grit Size D_g(μm)	STD D_g(μm)	Grit Radius R(μm)	L_g Grit Spacing(μm)	STD L_g(μm)
DWS3	304	3	78	9	39	280	104
DWS5	252	3	27	5	13.5	69	31

2.4 Vibration Assistance Setup

Subsurface damage could be reduced by vibration-assisted cutting, because intermittent unloading can produce a lateral crack before the median crack fully develops, and upon reloading, the lateral crack shields against further median crack penetration, as shown in Fig. 2.4. When the cutting grit first contacts the work piece, the median crack 1 is produced, after the grit unloads, the lateral crack 2 initiate, and then reloading the work piece produces the median crack 3. At this instant, the lateral crack 2 acts as a barrier against further penetration of the median crack, thus achieving the shielding effect. Furthermore, intermittent unloading produces shielding even for oblique indentation events and intermediate locations of lateral cracks. To investigate the beneficial effects of intermittent unloading, vibration-assisted cutting tests and no vibration-assisted cutting tests were carried out and compared. For vibration-assisted cutting tests, PMN-PT single crystal sample was fixed in the work table vertically by a clamping apparatus while the ultrasonic vibration-assisted device was located in horizontally and parallel to the wire running direction with its tip contacting with the left side of the clamping apparatus as can be seen in Fig. 2.5.

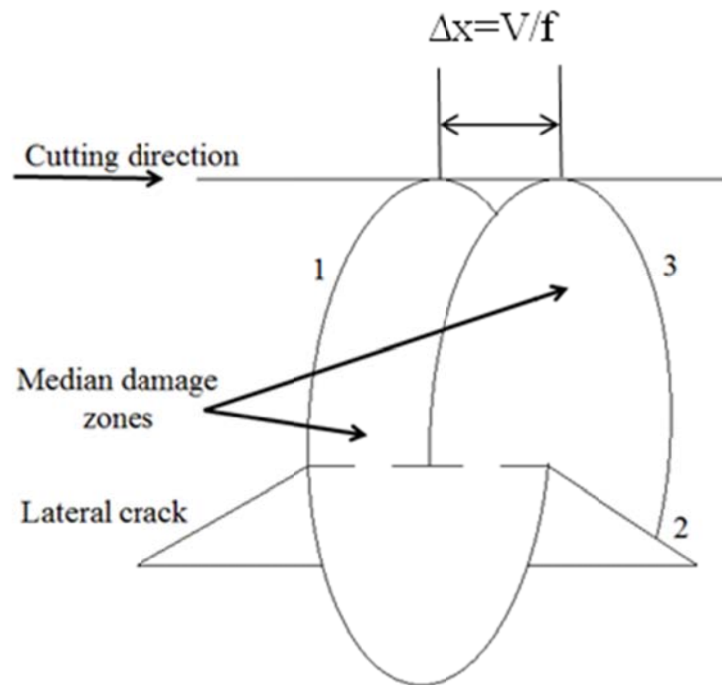

Fig. 2.4 Schematic diagram shows the shielding effect

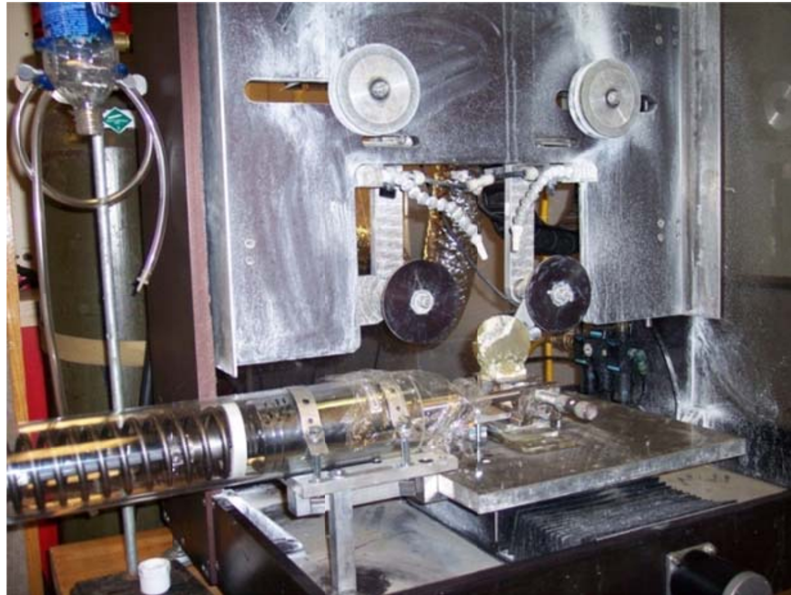

Fig. 2.5 Optical image shows the vibration-assisted cutting process

2.5. Preliminary Results

The goal of this study is to investigate the role of the wire saw process parameters on the quality of the produced surfaces, as measured by the resultant surface roughness and waviness, surface and subsurface crack length, damage; the role of the vibration cutting on possible phase transformation, as analyzed by XRD and Raman Spectrum.

2.5.1 Roughness Evolution

The surface roughness of the cut surfaces was measured using an optical non-contact profilometer, Zygo New View 6000, manufactured by Zygo Corporation. A 10x lens was used for the measurements. The profilometer has a resolution of depth on the order of three nano- meter; the resolution in the horizontal plane is 1.1 μm, while the field of view used is 0.7x0.53 mm.

In a stitch measurement, the profilometer took continuous measurements each 0.7×0.53 mm and stitched them together into one data set. Three stitch measurements, each of 0.7×3 mm dimensions, were applied in the direction of cutting for each sample on the left-middle-right of the cut surface. After the measurements were taken, the data was processed using the software MetroPro Version 8.1.5 developed by Zygo company. A high pass filtering was applied to remove the surface waviness. The cutoff length was set at 0.8 mm. Arithmetic average deviation from the centerline (best fit plane) was obtained. The average of three measurements was taken as surface roughness of the test.

A Scanning Electron Microscope (SEM), JEOL JSM-606LV, was used to image the cut-surface topology. The SEM images were taken from the lower half of the sample, on the center line of the cut surface.

Ductile material removal and brittle fracture was observed in SEM images. The condition of point contact between the impregnated diamond and PMN-PT single crystal sample was presumed during wire saw cutting process, generally as the same as indentation process.

As discussed by Evans and Marshall [19], removal of plastically deformed material in the cutting zone reduces residual stress. This reduces the tendency of lateral crack formation in brittle materials. The median crack depth, *c*, can be compared to measured roughness. Fu et al. [20] derived the force on a single grit in ductile mode material removal as presented in Eq. 2.2**,** where σ_y is yield stress, *R* is cutting particle radius, and *h* is cut depth for a single particle.

$$P = F_{zg} = 2\pi\sigma_y Rh \tag{2.2}$$

The mass continuity of the cutting process gives us Eq. 2.3.

$$V_z = \frac{d}{dt}\left(\frac{Volume}{A_p}\right) = \frac{d}{dt}\left(\frac{\frac{L_o}{L_g} \times D \times h \times S}{L_o \times D}\right) = \frac{dS}{dt}\left(\frac{h}{L_g}\right) = V_x\left(\frac{h}{L_g}\right) \tag{2.3}$$

Volume is the total amount of material removed, A_p is the projected area of the cut trench, L_o is the cut length of sample, L_g is the distance between cutting particles, *D* is width of cut trench that can be taken as diameter of wire, *S* is sliding distance, V_x is the axial speed of wire, and V_z is the feed of wire. Solving the cut depth *h* from Eq. 2.3 yields Eq. 2.4.

$$h = L_g \times \frac{V_z}{V_x} \tag{2.4}$$

The force on a single grit, F_{zg}, can be obtained in terms of process parameters by inserting Eq.2.4 into Eq. 2.2 and Eq. 2.5 is obtained.

$$P = F_{zg} = 2\pi\sigma_y R L_g \times \frac{V_z}{V_x} \tag{2.5}$$

The damage resulting from wire saw cutting is correlated with median crack depth. Lawn et al. [21] derived the median crack length using fracture mechanics principles. The median crack length is presented in Eq. 2.6.

$$C = \left[\alpha(\cot\psi)^{\frac{2}{3}}\left(\frac{E}{H}\right)^{\frac{1}{2}}\frac{P}{K_c}\right]^{\frac{2}{3}} \tag{2.6}$$

Inserting Eq. 2.5 into Eq. 2.6 gives us Eq. 2.7.

$$C = \left[\alpha(\cot\psi)^{\frac{2}{3}}\left(\frac{E}{H}\right)^{\frac{1}{2}}\frac{2\pi\sigma_y R L_g}{K_c}\right]^{\frac{2}{3}}\left[\frac{V_z}{V_x}\right]^{\frac{2}{3}} \tag{2.7}$$

The median crack depth, which is the damage due to the wire saw process, is presented in terms of the process parameters in Eq. 2.7. The damage is a function of the half of the included angle of the grits, ψ; the modulus of elasticity of ingot, E; the hardness of the ingot, H; the fracture toughness of the ingot, K_c; wire properties, feed speed, and wire speed.

The damage model states that under the same feed speed, if the wire speed is increased, the roughness damage will increase, which can be seen in Fig. 2.6, and the 3D images of surface roughness are shown in Fig. 2.7. The results also show that sample wafers cut by wire DWS5 is more roughness, that's because compared with the wire DWS3, the average impregnated diamond size, average spacing of abrasive grits, and wire cross-section diameter of wire DWS5 is much smaller, scratch between the wire DWS5 and the PMN-PT single crystals is more seriously. When combined with vibration assistance, the intermittent unloading can produce a lateral crack before the median crack fully develops, and upon

reloading, the lateral crack shields against further median crack penetration, so the vibration assisted-cutting can get smoother surface.

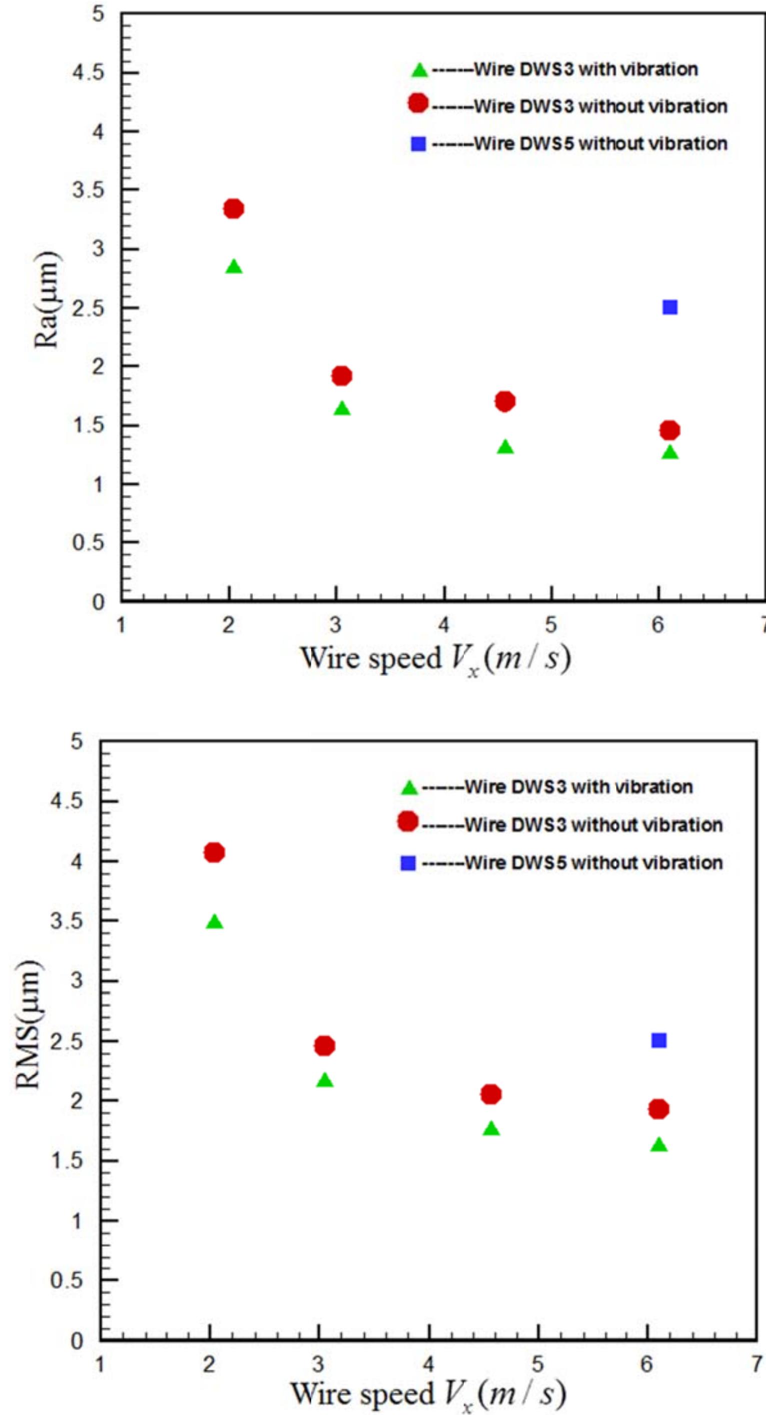

Fig. 2.6 The variation of surface roughness Ra and RMS as a function of V_x
(V_z=6.35 µm/sec, T=13N)

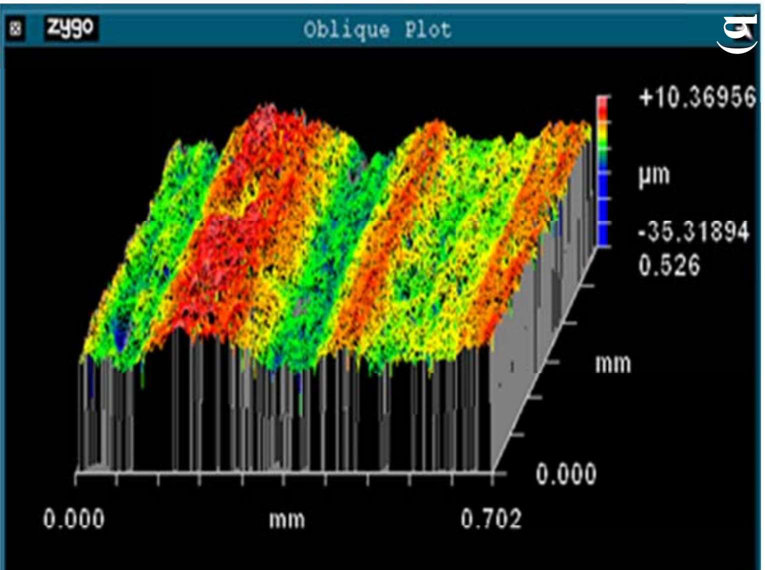
b)
Oblique Plot
+10.36956
µm
-35.31894
0.526
mm
0.000
0.000
mm
0.702

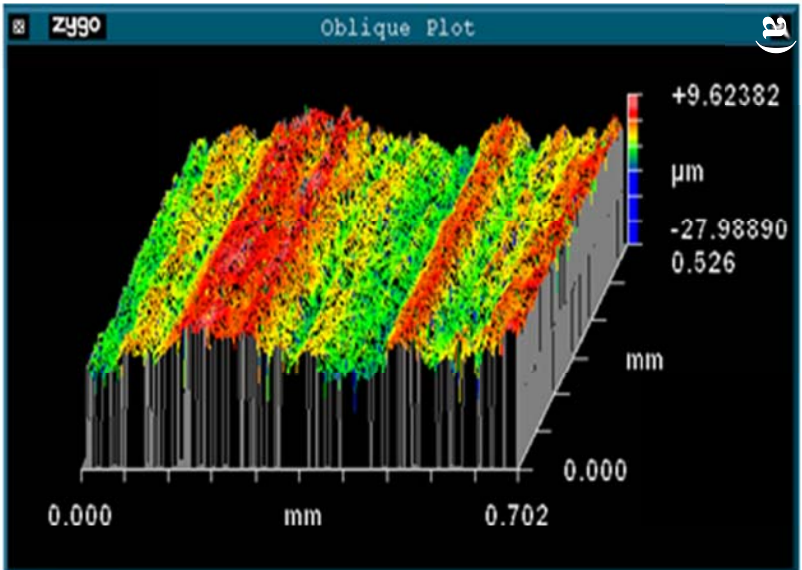
a)
Oblique Plot
+9.62382
µm
-27.98890
0.526
mm
0.000
0.000
mm
0.702

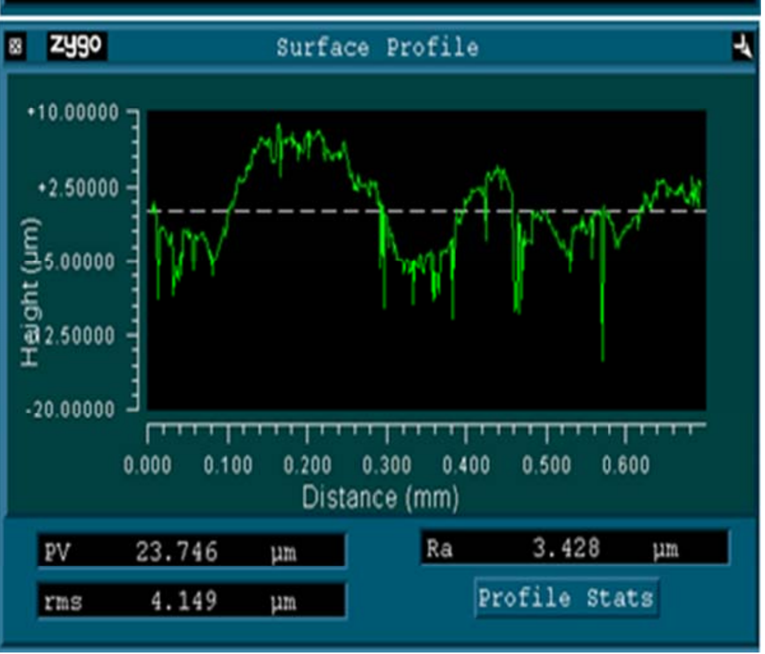
Surface Profile
Height (µm)
Distance (mm)
PV 23.746 µm
rms 4.149 µm
Ra 3.428 µm
Profile Stats

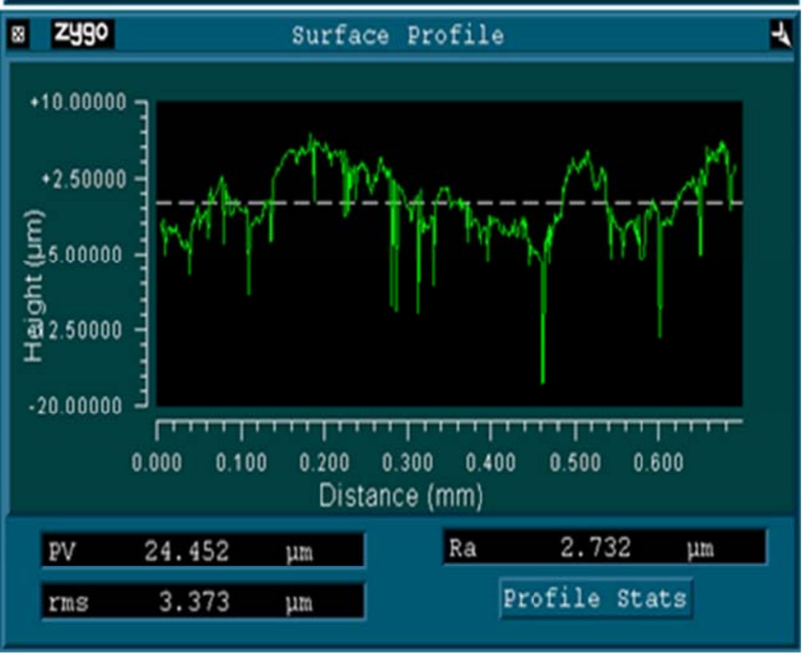
Surface Profile
Height (µm)
Distance (mm)
PV 24.452 µm
rms 3.373 µm
Ra 2.732 µm
Profile Stats

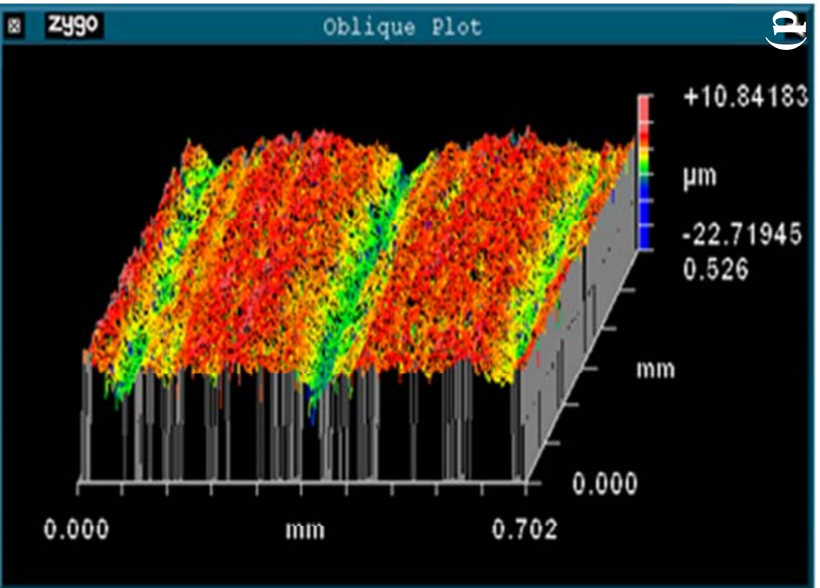
zygo
Oblique Plot
d)
+10.84183
µm
-22.71945
0.526
mm
0.000
0.000
mm
0.702

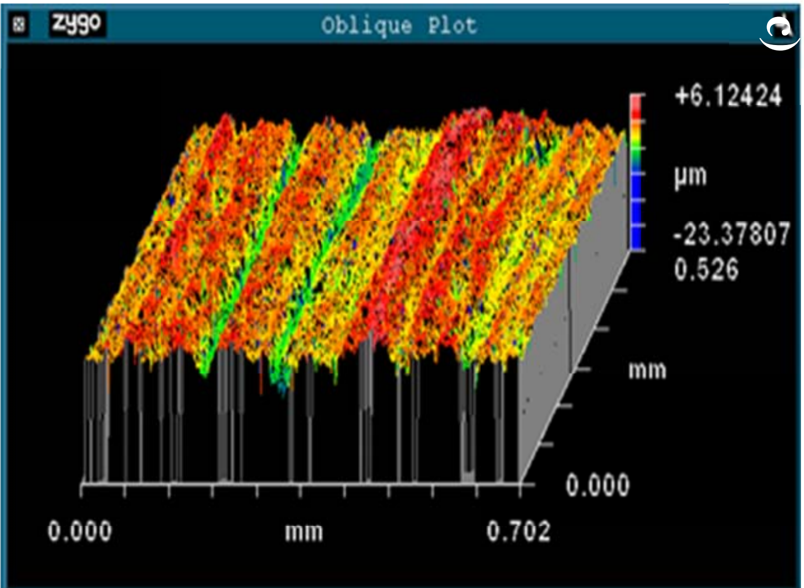
zygo
Oblique Plot
c)
+6.12424
µm
-23.37807
0.526
mm
0.000
0.000
mm
0.702

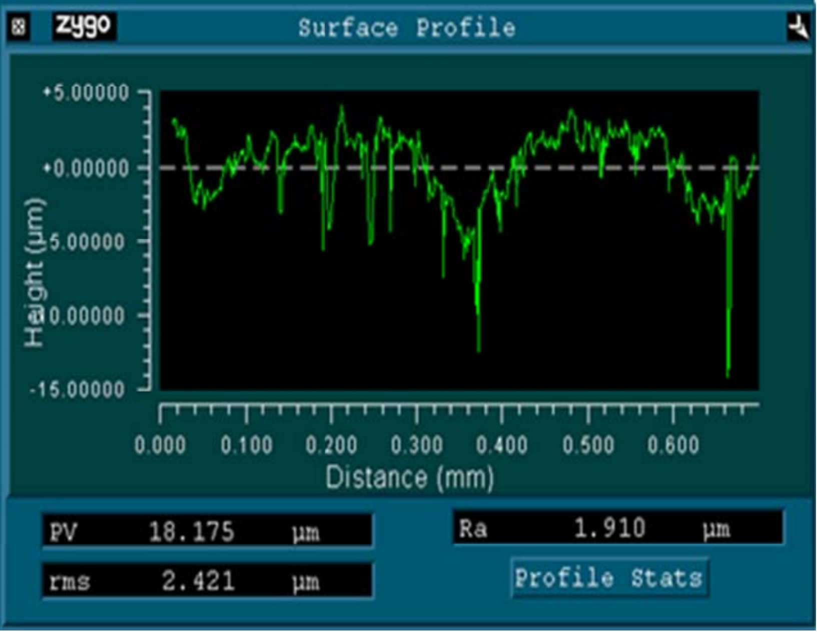
zygo
Surface Profile
Height (µm)
Distance (mm)
PV 18.175 µm
rms 2.421 µm
Ra 1.910 µm
Profile Stats

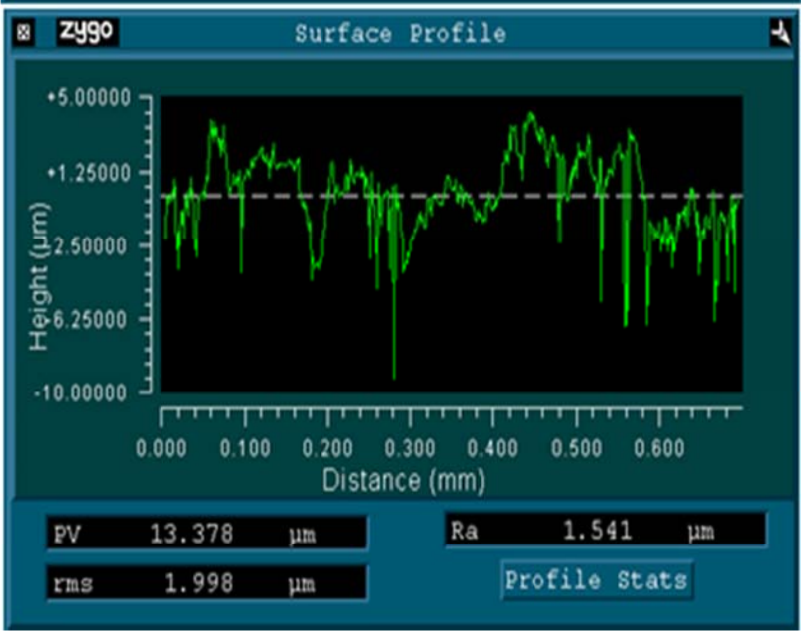
zygo
Surface Profile
Height (µm)
Distance (mm)
PV 13.378 µm
rms 1.998 µm
Ra 1.541 µm
Profile Stats

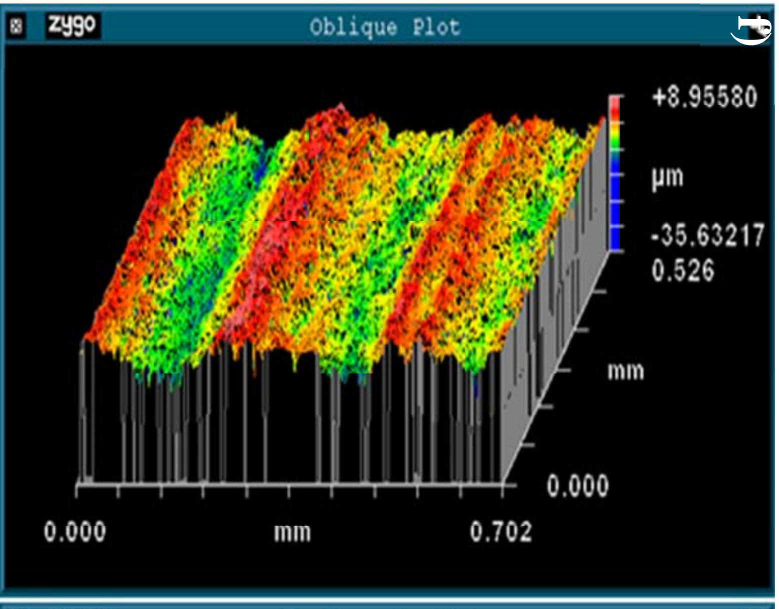
Oblique Plot
+8.95580
µm
-35.63217
0.526
mm
0.000
0.000
mm
0.702

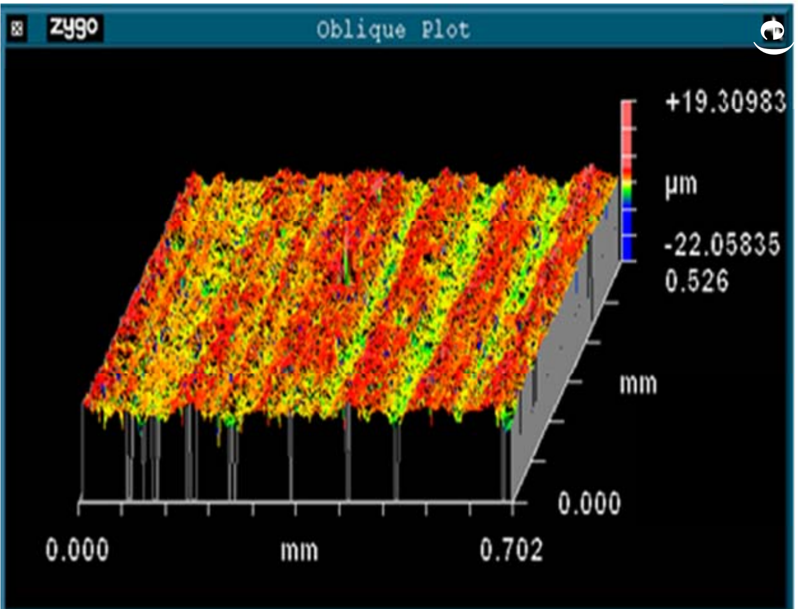
Oblique Plot
+19.30983
µm
-22.05835
0.526
mm
0.000
0.000
mm
0.702

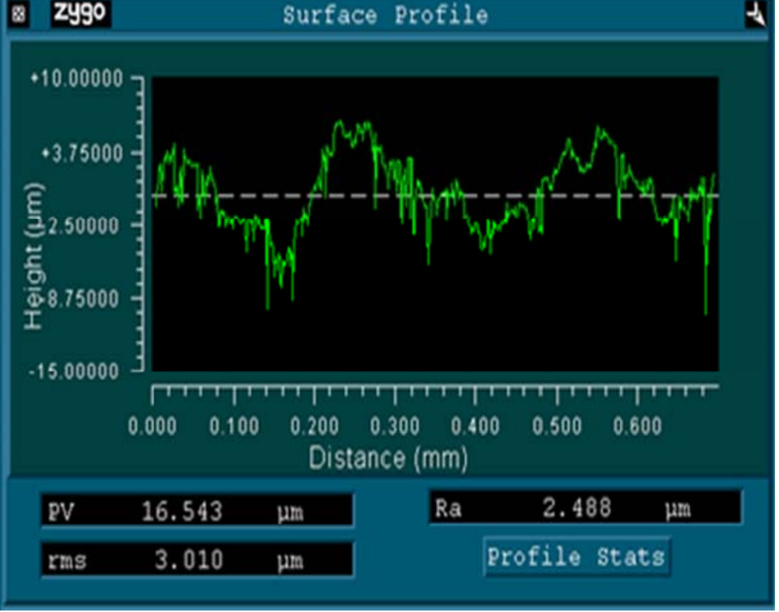
Surface Profile
+10.00000
+3.75000
2.50000
8.75000
-15.00000
Height (µm)
0.000 0.100 0.200 0.300 0.400 0.500 0.600
Distance (mm)
PV 16.543 µm
rms 3.010 µm
Ra 2.488 µm
Profile Stats

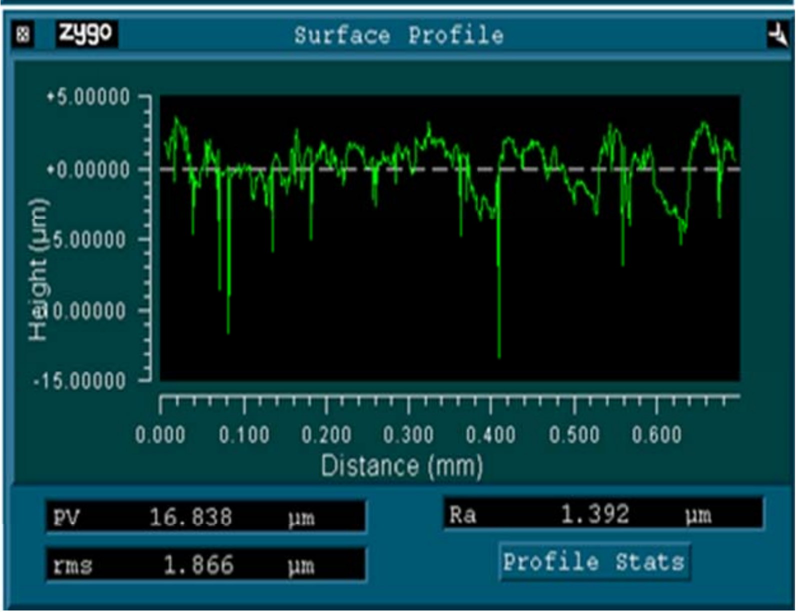
Surface Profile
+5.00000
+0.00000
5.00000
0.00000
-15.00000
Height (µm)
0.000 0.100 0.200 0.300 0.400 0.500 0.600
Distance (mm)
PV 16.838 µm
rms 1.866 µm
Ra 1.392 µm
Profile Stats

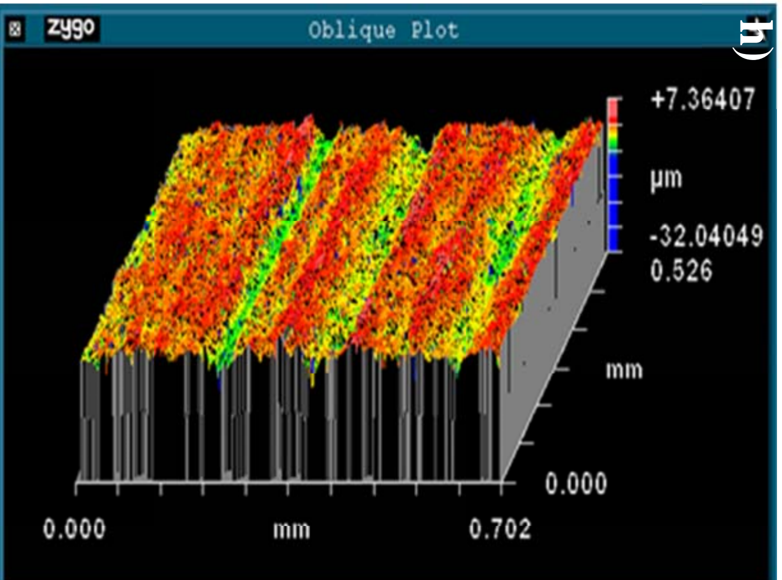
h)
Oblique Plot
+7.36407
µm
-32.04049
0.526
mm
0.000
0.000
mm
0.702

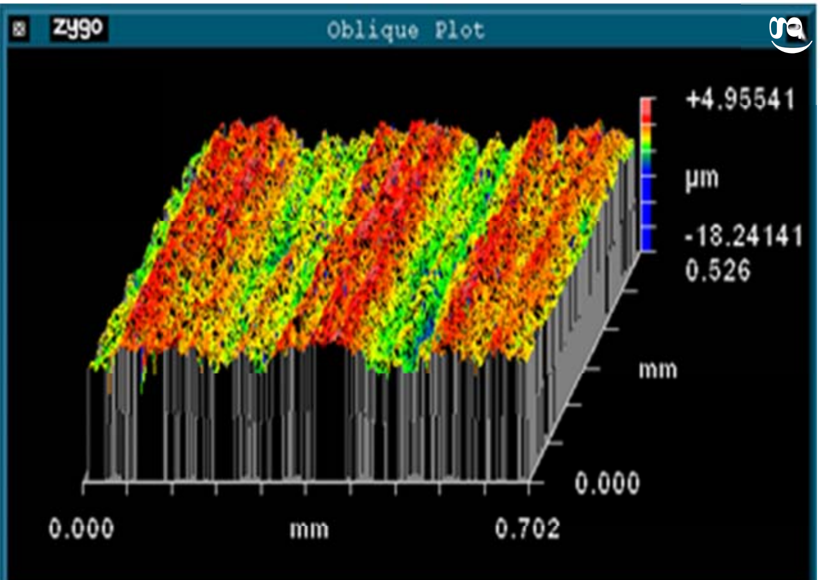
g)
Oblique Plot
+4.95541
µm
-18.24141
0.526
mm
0.000
0.000
mm
0.702

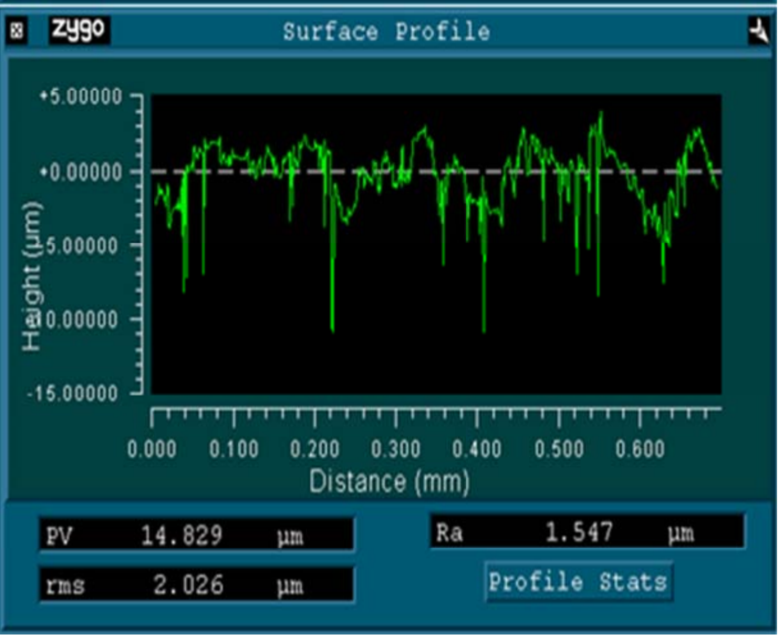
Surface Profile
Height (µm)
Distance (mm)
PV 14.829 µm
rms 2.026 µm
Ra 1.547 µm
Profile Stats

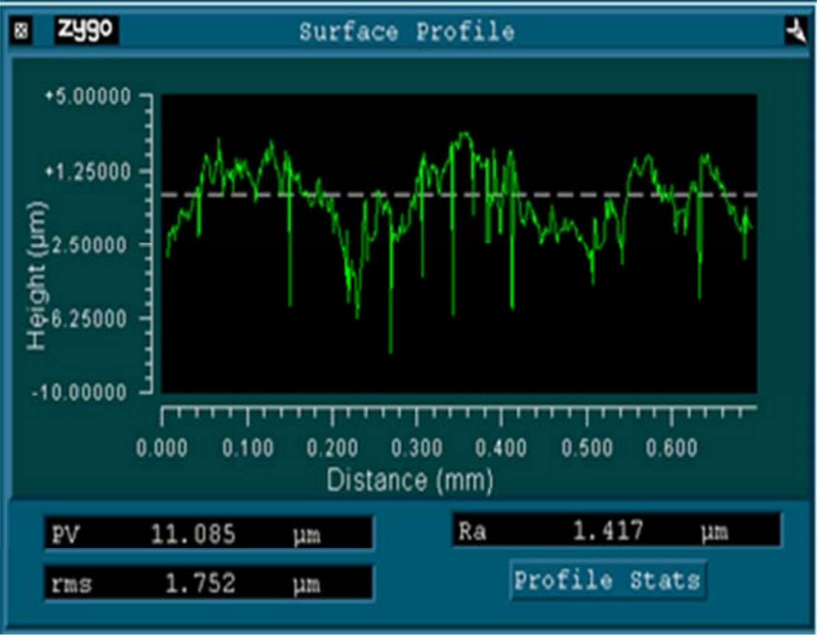
Surface Profile
Height (µm)
Distance (mm)
PV 11.085 µm
rms 1.752 µm
Ra 1.417 µm
Profile Stats

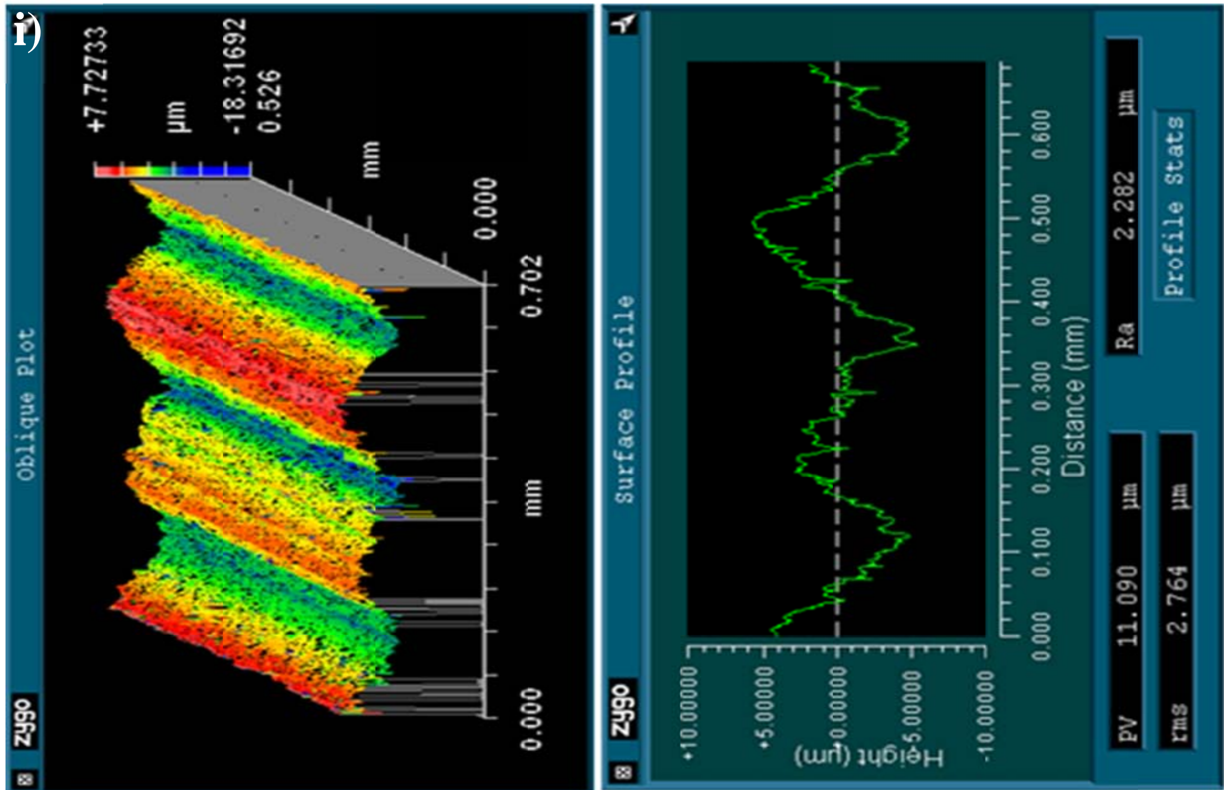

Fig.2.7. 3D surface reconstruction images show wire saw cut surfaces roughness as measured by Zygo profilometer: **a)** DWS3 wire with vibration, V_x=2 m/s; **b)**DWS3 wire without vibration, V_x=2 m/s; **c)** DWS3 wire with vibration, V_x=3.05 m/s; **d)** DWS3 wire without vibration, V_x=3.05 m/s; **e)** DWS3 wire with vibration, V_x=4.57 m/s; **f)** DWS3 wire without vibration, V_x=4.57 m/s; **g)** DWS3 wire with Vibration, V_x=6.1 m/s; **h)** DWS3 wire without vibration, V_x=6.1 m/s; **i)** DWS5 wire without Vibration, V_x=6.1 m/s ($V_Z = 6.35\ \mu m/sec, T = 13N$).

The same results are shown in Fig.2.8, there are more scratches on the wire saw cutting surface processed by wire DWS5 than cut by wire DWS3, while all of the other cutting parameters are the same. If the same type of wire is chosen, with the decrease of wire cutting speed, the final sample wafers surfaces are more roughness, since more scratches are presented and the length of medial cracks is much larger. The length of medial cracks under cutting with vibration assistance is smaller than cutting without vibration assistance, and the surfaces are also more smoothly.

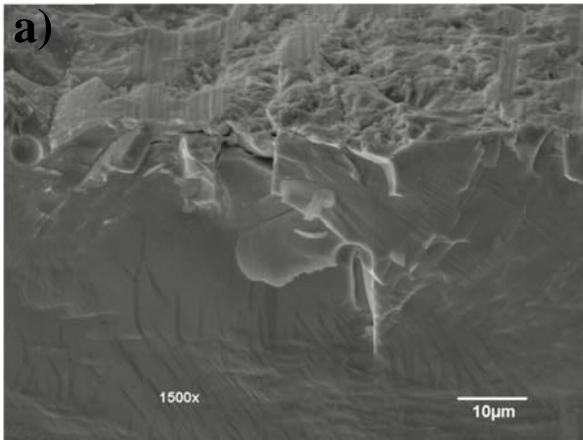
a)
1500x
10µm

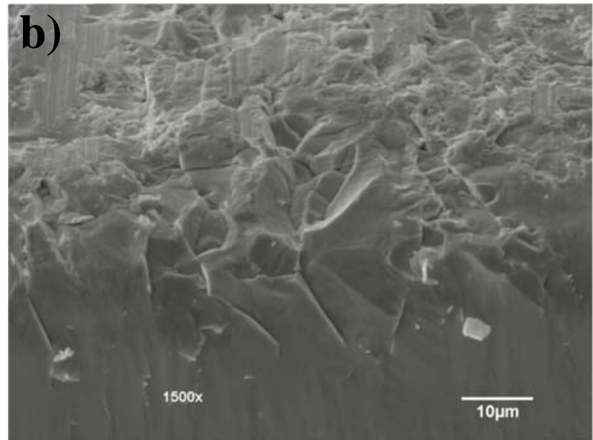
b)
1500x
10µm

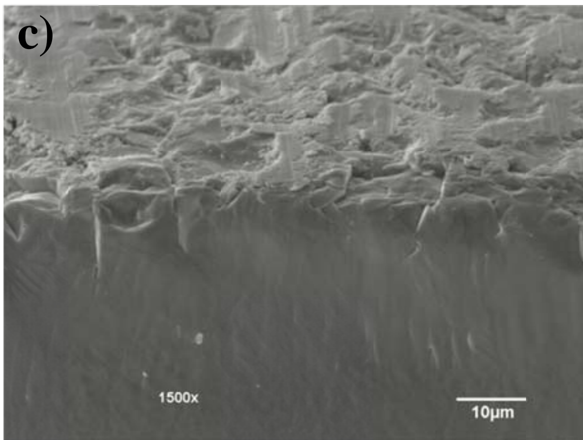
c)
1500x
10µm

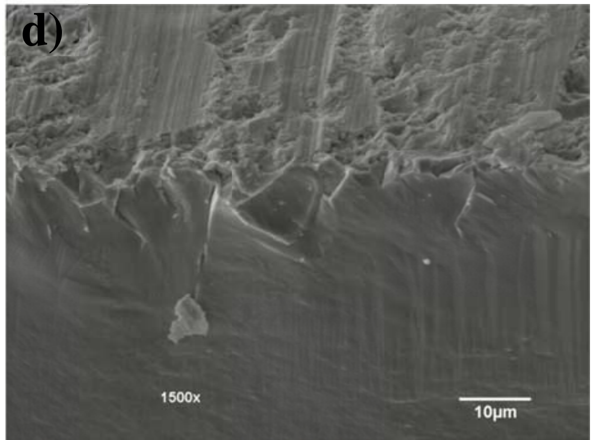
d)
1500x
10µm

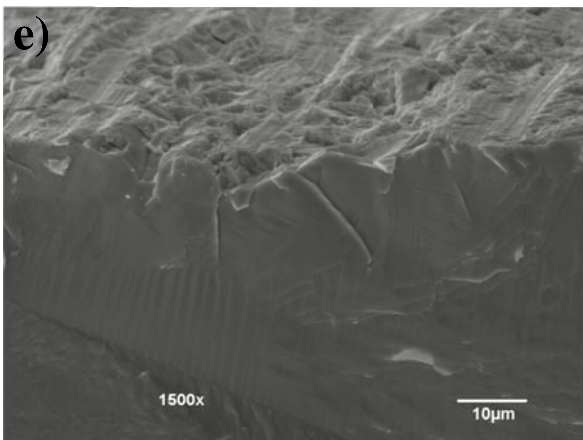
e)
1500x
10µm

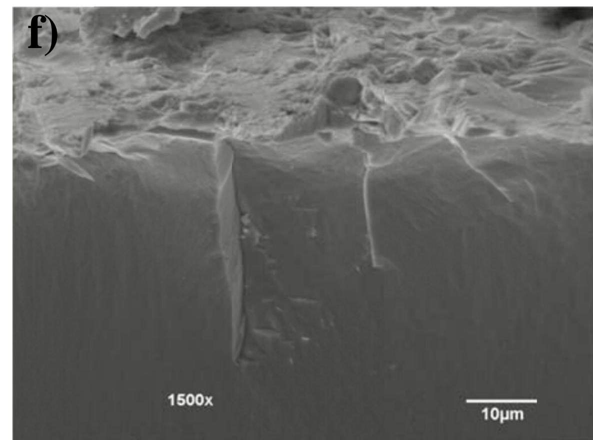
f)
1500x
10µm

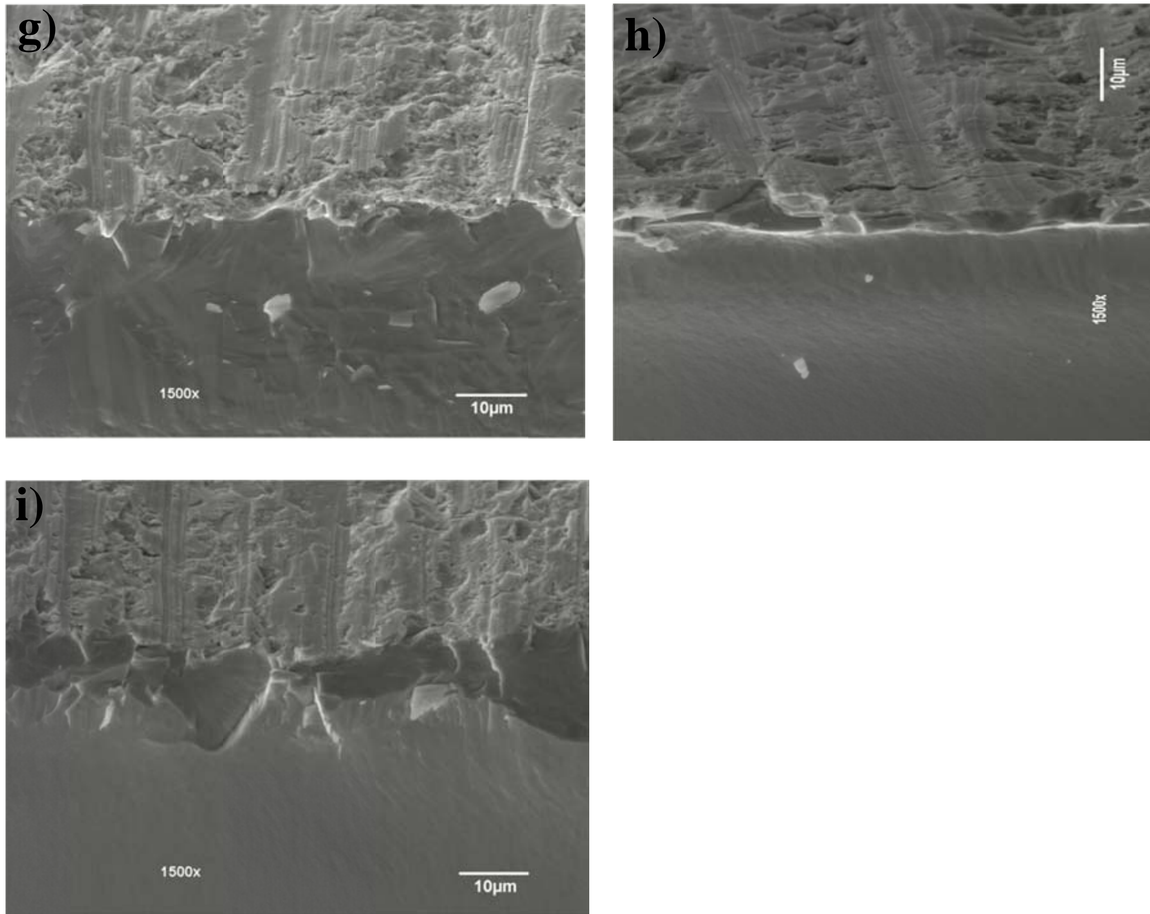

Fig.2.8. SEM images of wire saw cut surfaces: **a)** DWS3 wire with vibration, V_x=2 m/s; **b)**DWS3 wire without vibration, V_x=2 m/s; **c)** DWS3 wire with vibration, V_x=3.05 m/s; **d)** DWS3 wire without vibration, V_x=3.05 m/s; **e)** DWS3 wire with vibration, V_x=4.57 m/s; **f)** DWS3 wire without vibration, V_x=4.57 m/s; **g)** DWS3 wire with Vibration, V_x=6.1 m/s; **h)** DWS3 wire without vibration, V_x=6.1 m/s; **i)** DWS5 wire without Vibration, V_x=6.1 m/s ($V_Z = 6.35\ \mu m/sec, T = 13N$).

2.5.2 Waviness Evolution

The surface waviness of the cut surfaces was measured using an optical non-contact profilometer, Zygo New View 6000, manufactured by Zygo Corporation. A 2.5x lens with 2x zoom was used for the measurements. The profilometer has a vertical resolution on the order of 3 nano-meter; the resolution in the horizontal plane is 8.83 μm, while the field of view used is 1.41×1.06 mm.

In a stitch measurement, the profilometer took continuous measurements of 1.41×1.06 mm and stitches them together into one data set. A low pass filtering was applied, and the cutoff length was set at 0.25 mm. Stitch measurements were applied in the direction of cutting at the center of the cut surface for each sample. After the measurements were taken, the data was processed using the software Metro Pro Version 8.1.5 developed by Zygo company. The best fit plane was removed and a low pass filter was applied to get the waviness profile of the cut surface.

The long waviness is induced by the wire drifting that influenced by the combination of the oblique cutting force and wire tension, and also the increase of feed speed means the increase of oblique cutting forces will lead to a high peak-to-valley value waviness in the surface. The increase of the wire tension will lead to a wavy surface with a lower peak-to-valley value, while decreasing wire tension will lead to a step-like surface with a high peak-to-valley value. But as the same as roughness, under the same feed speed and wire tension, we can see smaller Ra and RMS of waviness with the increase of cutting speed and better condition when combined with vibration assistance as shown in Fig. 2.9, since Ra and RMS is only the performance that related to cracks initiation, propagation and if scratch seriously or not. The 3D images of surface waviness are shown in Fig. 2.10.

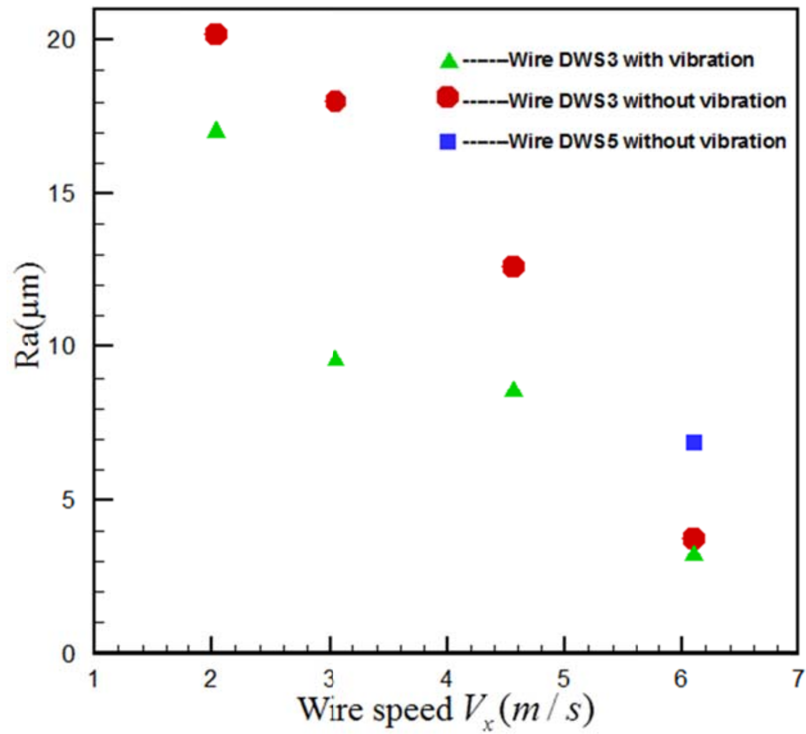

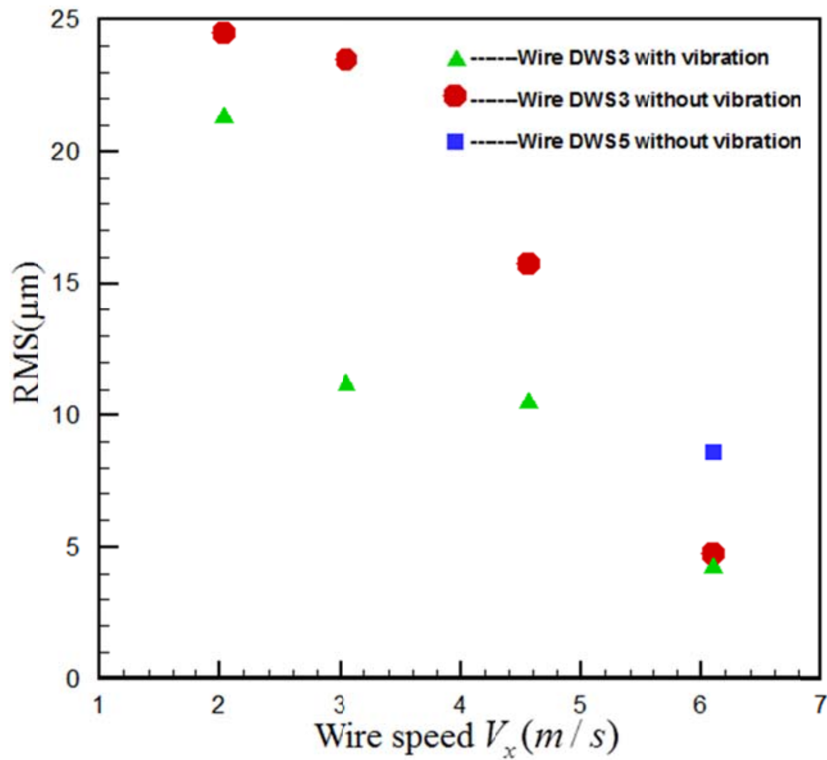

Fig. 2.9 The variation of surface waviness Ra and RMS as a function of V_x (V_z=6.35 μm/sec, T=13N)

zygo
Oblique Plot
a)
+92.199
µm
-36.1194
0.00
mm
17.54

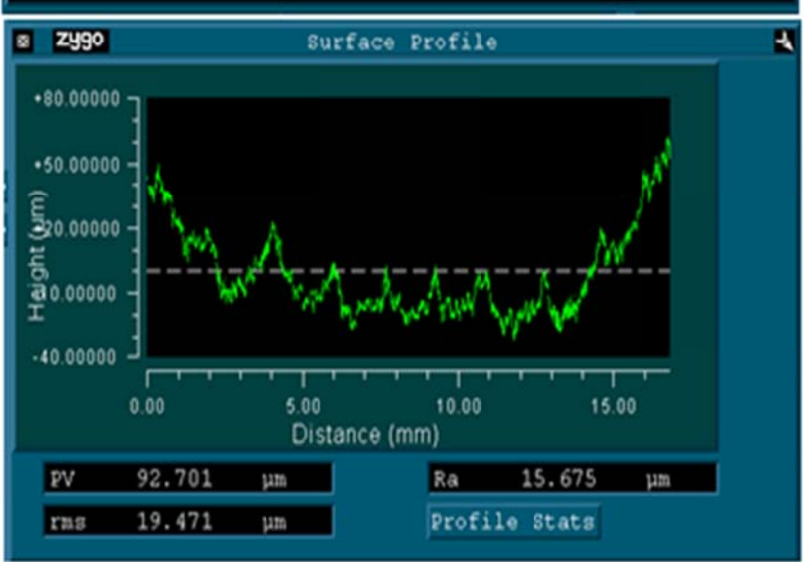
zygo
Surface Profile
+80.00000
+50.00000
20.00000
0.00000
-40.00000
Height (µm)
0.00
5.00
10.00
15.00
Distance (mm)
PV 92.701 µm
rms 19.471 µm
Ra 15.675 µm
Profile Stats

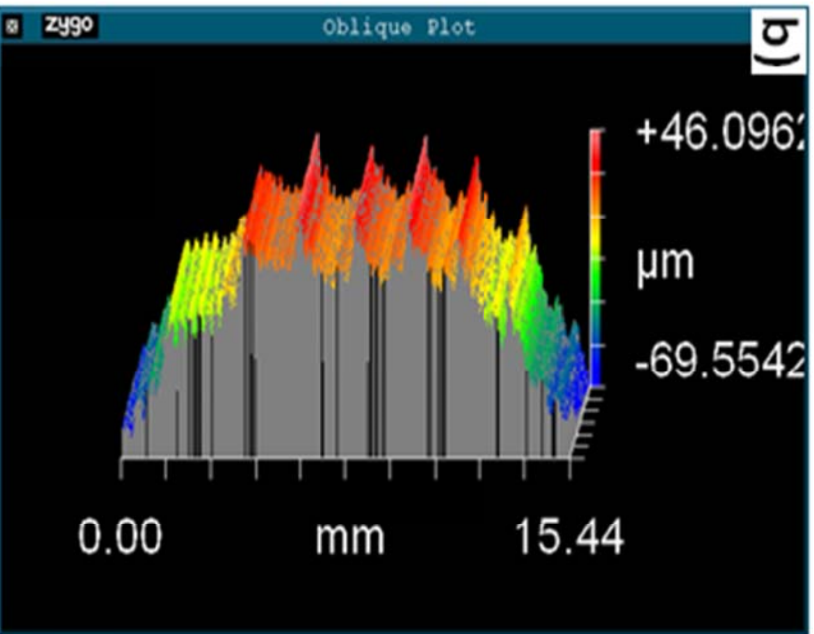
zygo
Oblique Plot
b)
+46.0962
µm
-69.5542
0.00
mm
15.44

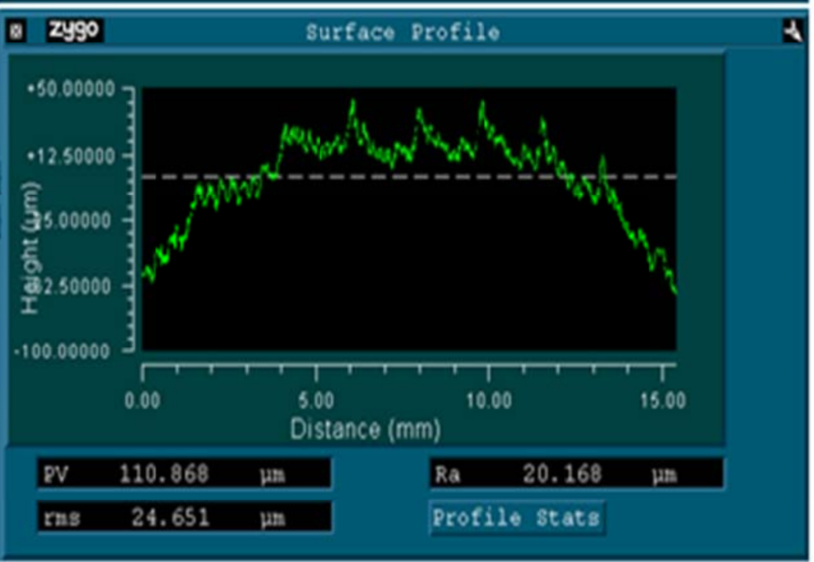
zygo
Surface Profile
+50.00000
+12.50000
-100.00000
Height (µm)
0.00
5.00
10.00
15.00
Distance (mm)
PV 110.868 µm
rms 24.651 µm
Ra 20.168 µm
Profile Stats

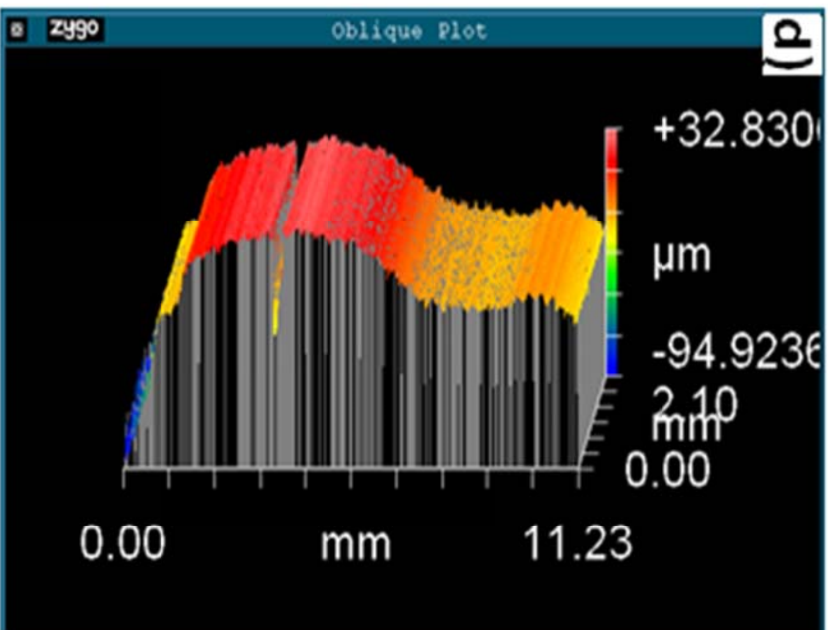
d)
zygo
Oblique Plot
+32.830
µm
2.10
mm
0.00
0.00
mm
11.23

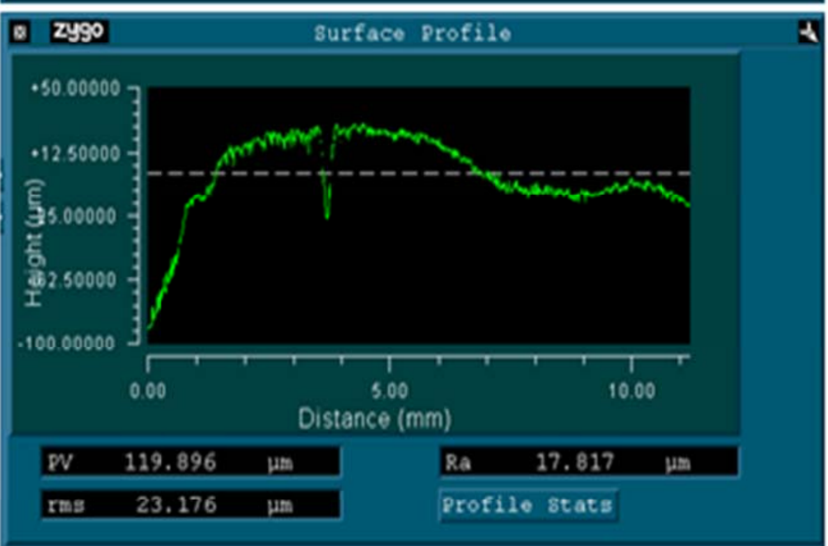
zygo
Surface Profile
+50.00000
+12.50000
-100.00000
Height (µm)
0.00
5.00
10.00
Distance (mm)
PV 119.896 µm
rms 23.176 µm
Ra 17.817 µm
Profile Stats

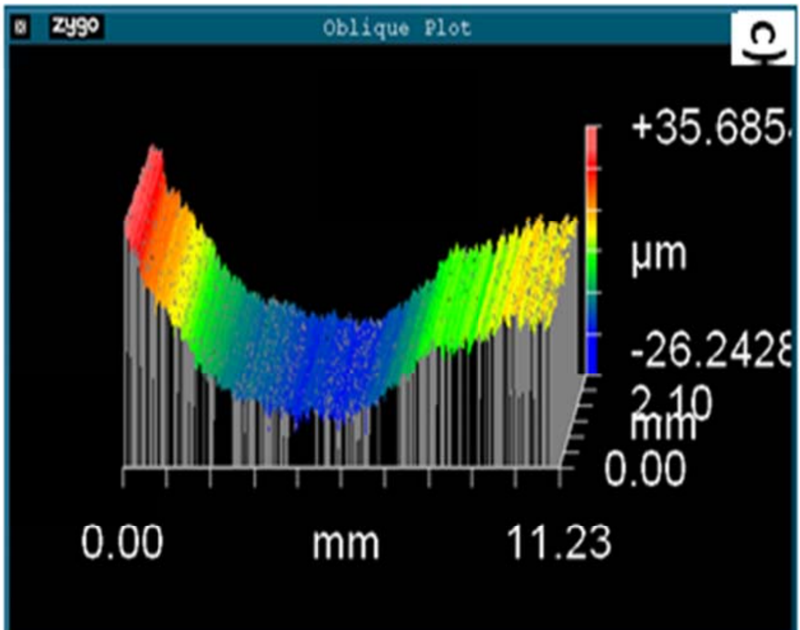
c)
zygo
Oblique Plot
µm
2.10
mm
0.00
0.00
mm
11.23

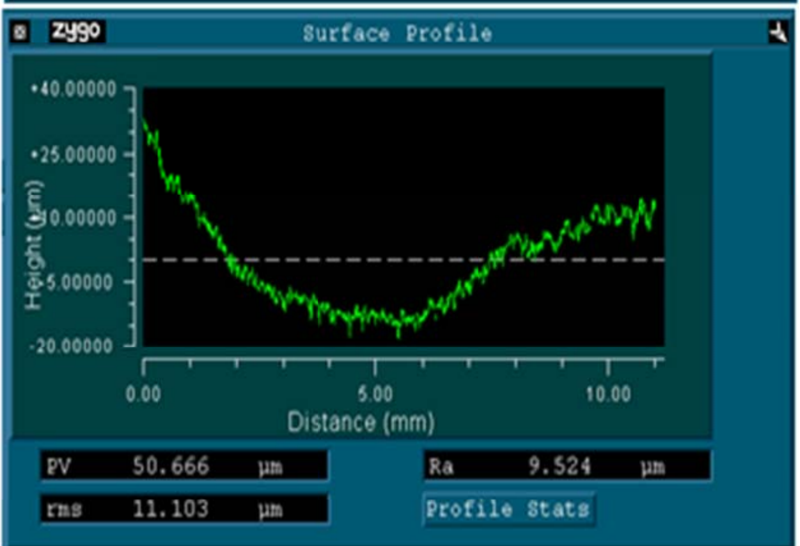
zygo
Surface Profile
+40.00000
+25.00000
-20.00000
Height (µm)
0.00
5.00
10.00
Distance (mm)
PV 50.666 µm
rms 11.103 µm
Ra 9.524 µm
Profile Stats

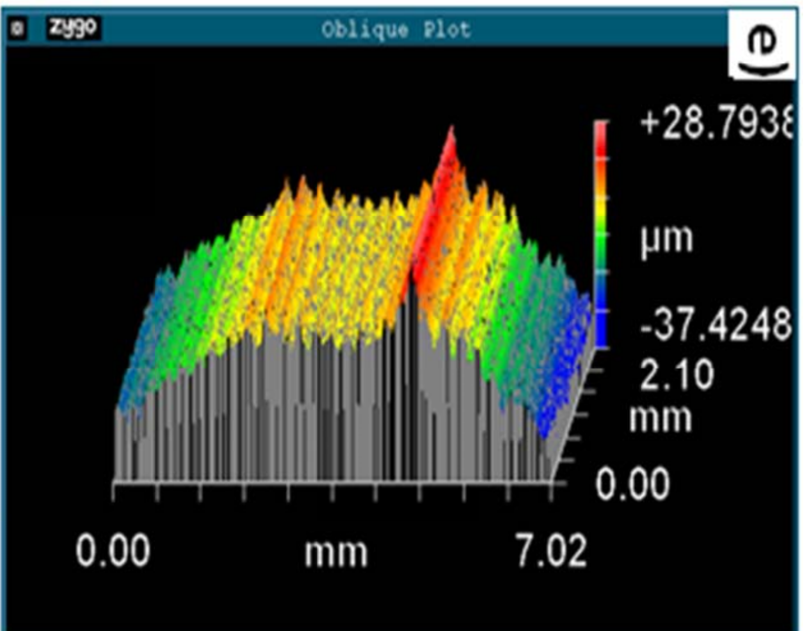

e)
Oblique Plot
+28.7938
µm
-37.4248
2.10
mm
0.00
0.00
mm
7.02

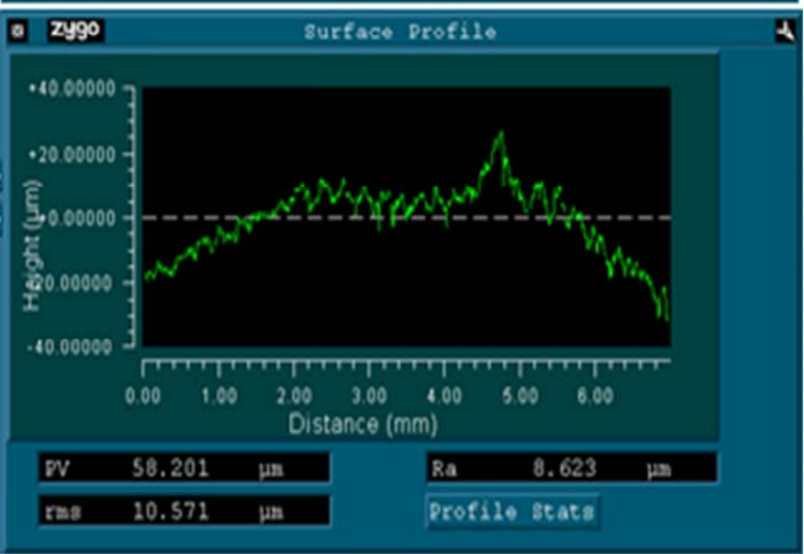

Surface Profile
Height (µm)
Distance (mm)
PV 58.201 µm
rms 10.571 µm
Ra 8.623 µm
Profile Stats

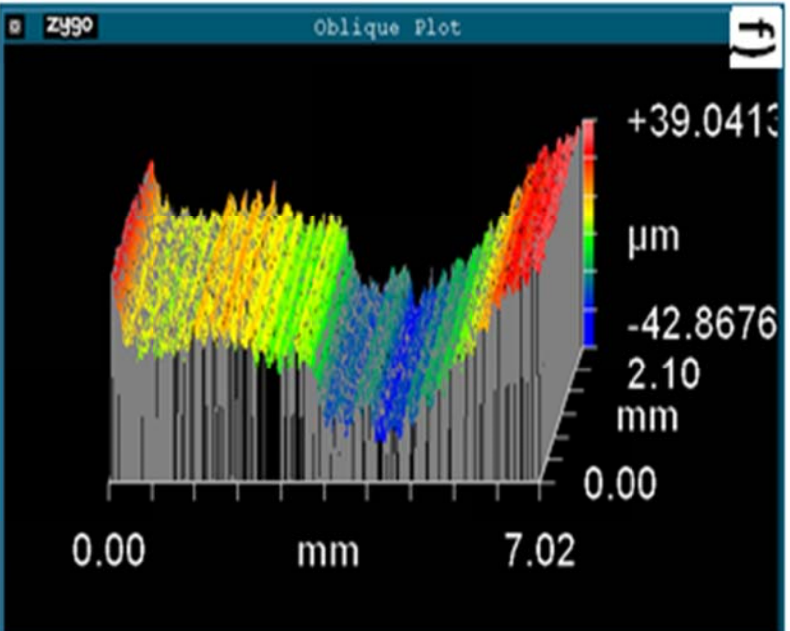

f)
Oblique Plot
+39.0413
µm
-42.8676
2.10
mm
0.00
0.00
mm
7.02

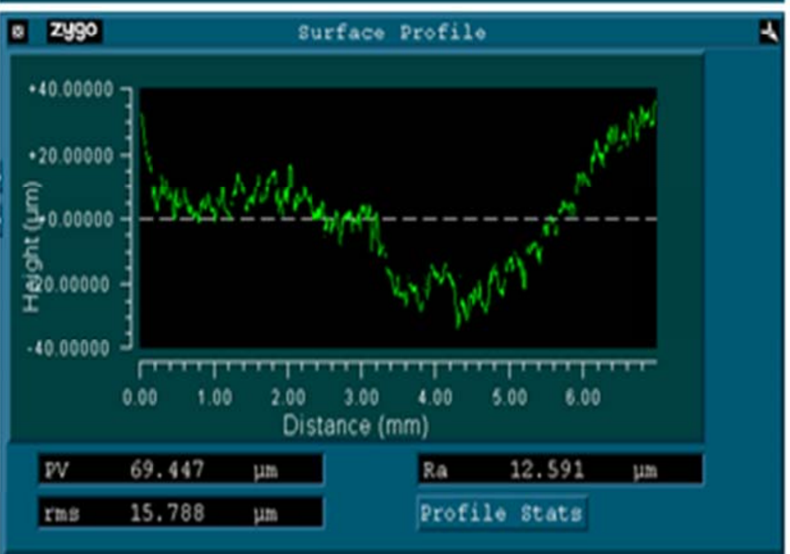

Surface Profile
Height (µm)
Distance (mm)
PV 69.447 µm
rms 15.788 µm
Ra 12.591 µm
Profile Stats

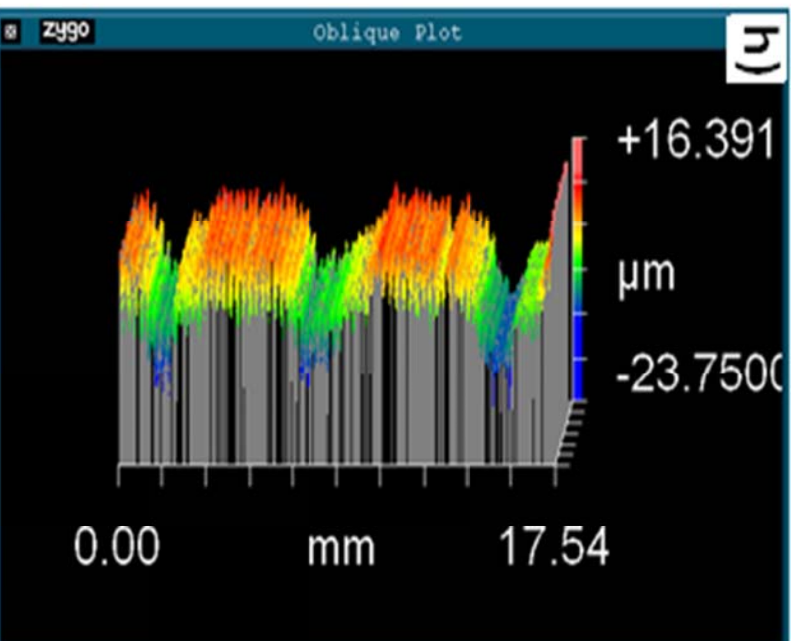
zygo
Oblique Plot
h)
+16.391
µm
0.00
mm
17.54

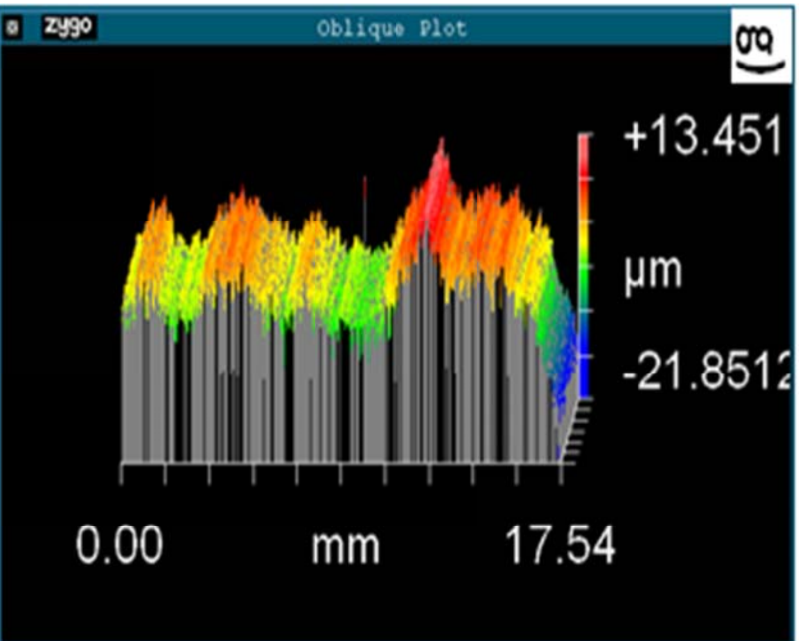
zygo
Oblique Plot
g)
+13.451
µm
0.00
mm
17.54

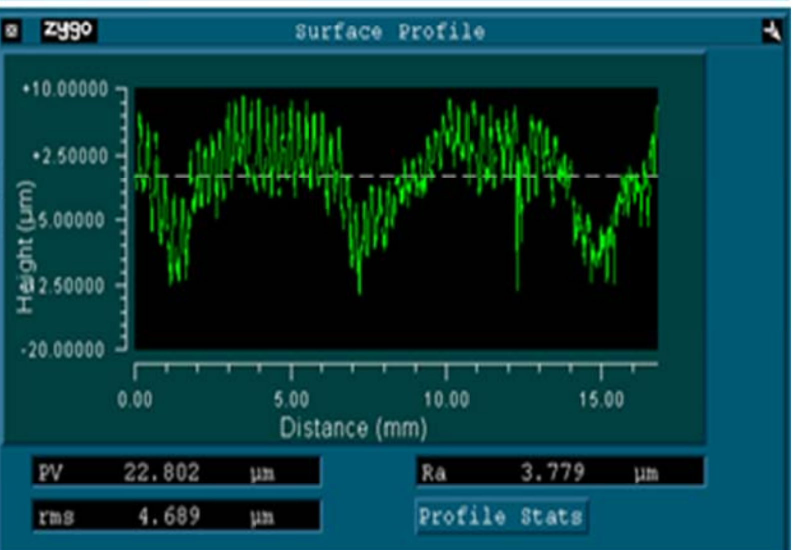
zygo
Surface Profile
Height (µm)
Distance (mm)
PV 22.802 µm
rms 4.689 µm
Ra 3.779 µm
Profile Stats

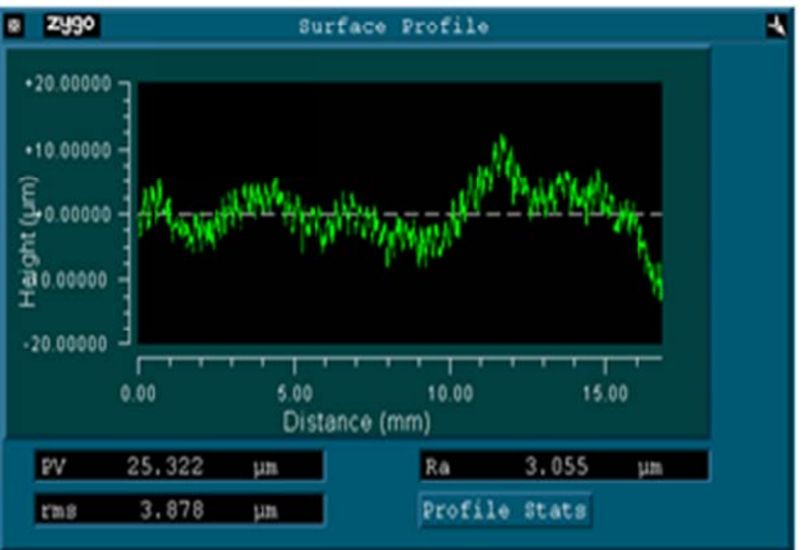
zygo
Surface Profile
Height (µm)
Distance (mm)
PV 25.322 µm
rms 3.878 µm
Ra 3.055 µm
Profile Stats

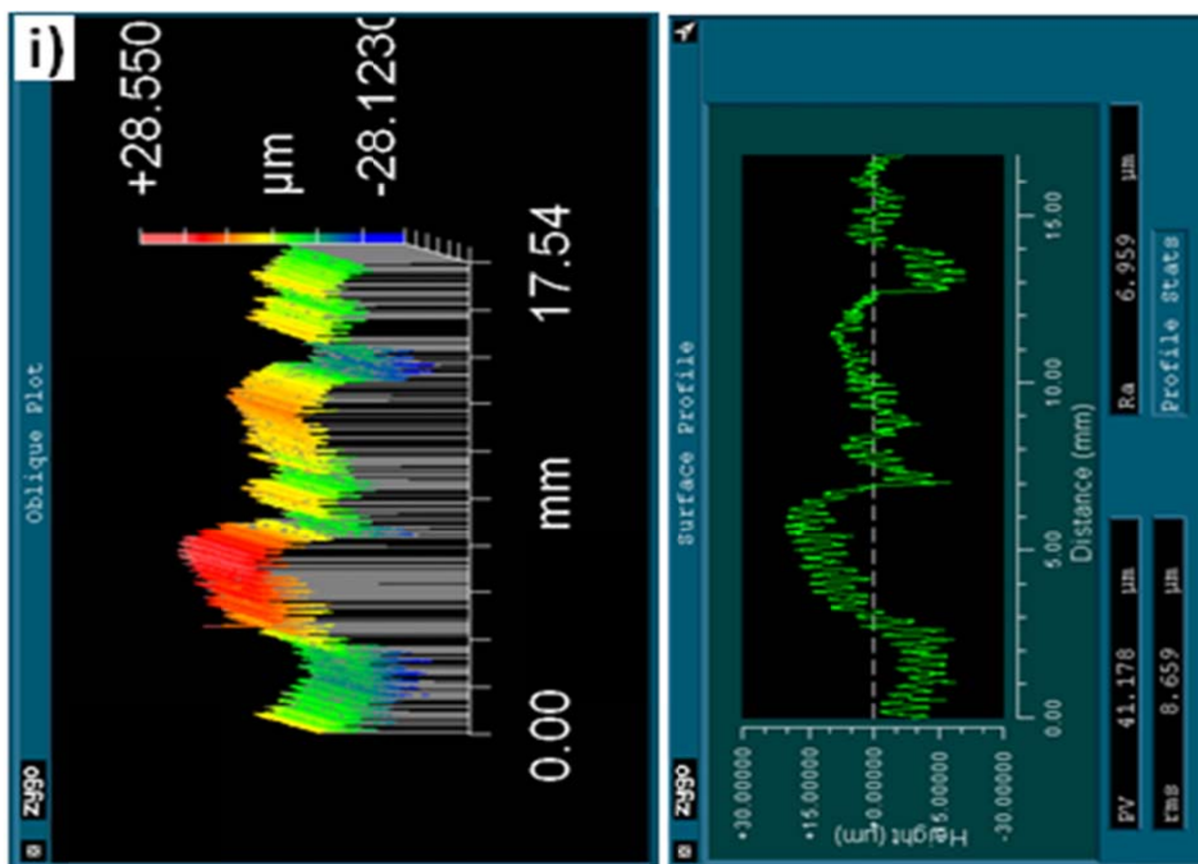

Fig.2.10. 3D surface reconstruction images show wire saw cut surfaces waviness as measured by Zygo profilometer: **a)** DWS3 wire with vibration, V_x=2 m/s; **b)**DWS3 wire without vibration, V_x=2 m/s; **c)** DWS3 wire with vibration, V_x=3.05 m/s; **d)** DWS3 wire without vibration, V_x=3.05 m/s; **e)** DWS3 wire with vibration, V_x=4.57 m/s; **f)** DWS3 wire without vibration, V_x=4.57 m/s; **g)** DWS3 wire with Vibration, V_x=6.1 m/s; **h)** DWS3 wire without vibration, V_x=6.1 m/s; **i)** DWS5 wire without Vibration, V_x=6.1 m/s ($V_Z = 6.35\ \mu m/sec, T = 13N$).

CHAPTER 3. PHASE TRANSFORMATION ANALYSIS

3.1 Introduction

Recent X-ray diffraction studies have shown that PMN-xPT single crystals at room temperature and at zero stress and zero electric field are in a rhombohedral phase when $x < 0.3$ and a tetragonal phase when $x > 0.35–0.37$ [22,23]. The region which separates the rhombohedral and tetragonal phase is called the morphotropic phase boundary (MPB). Studies have also shown that PMN-xPT and specimens near the morphotropic phase boundary (MPB) have an intricate multiphase state consisting of tetragonal, rhombohedral, orthorhombic and monoclinic phases M_A, M_B, M_C [23-25].

The phase of PMN-xPT is dependent on applied fields such as stress, electric field and temperature, in addition to the composition. The application of external stress fields can initiate phase transformations in relaxor PMN-xPT. Many researchers have shown experimental evidence of rhombohedral to orthorhombic (R–O) [26,27], rhombohedral to monoclinic (R-M) [28], and rhombohedral to tetragonal (R–T) [29] phase transformations in relaxor single crystals under external fields. In the region of PT percentage is no larger than 0.3($x \leq 0.3$), Viehland and Li [26] measured the unipolar and bipolar strain and electric displacement during electric field induced R–O phase transformation in <110> oriented PMN–0.3PT single-crystal specimens. McLaughlin et al. showed evidence that electric field [27] and stress fields [29] are both capable of inducing an R–O phase transformation in PMN–0.32PT single crystals with an engineered domain state, as seen in Fig.3.1. In this work, the electrical displacement and strain were measured as a function of stress, electric field and temperature. The results were presented as three-dimensional surface plots showing

the effects of field induced phase transformations. Phase transformation maps were created which showed the dependence of these transformations on applied electric field, stress and temperature. K.G. Webber et al. [30] showed evidence that a stress could drive the phase transformation from the rhombohedral phase to the depolarized orthorhombic phase in a single-crystal PMN-0.26PT, as seen in Fig.3.2, it shows the stress induced depolarization of the single-crystal material in the presence of an electric field well below the coercive field. During a unipolar stress cycle in the absence of an applied electric field it was shown that single-crystal PMN-0.26PT was driven to the depolarized orthorhombic phase. A. Slodczyk et al. [28] demonstrated that PMN-0.28PT underwent a transition from the cubic (P*m*3*m*) to the rhombohedral(R3*m*) at 348 K, and the rhombohedral(R3*m*) to the monoclinic symmetry (P*m*) in at 273K. Zhao et al. [31] confirmed an R–T phase transition in PMN–0.31PT single crystals with powder X-ray diffraction.

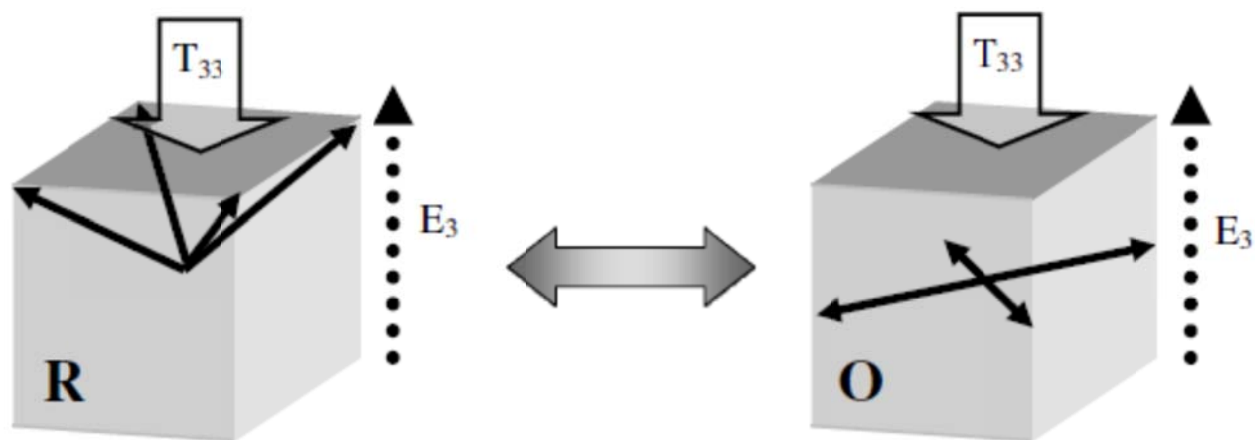

Fig. 3.1 Phase transformations between the rhombohedral and orthorhombic phases induced by stress. [29]

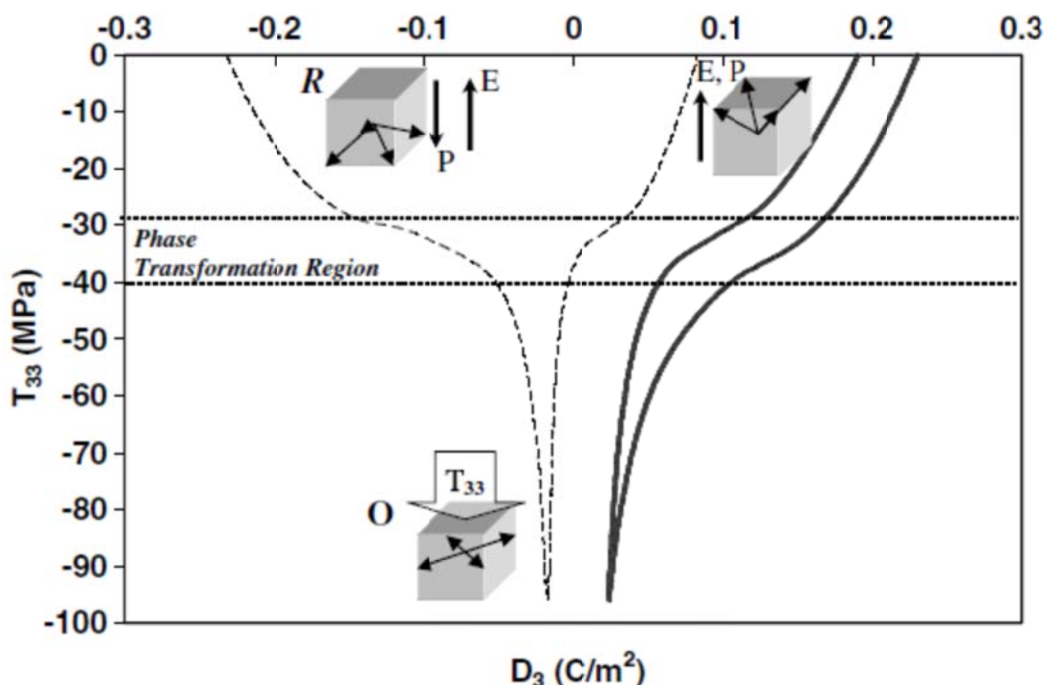

Fig. 3.2 The stress induced depolarization in the presence of a small bias electric field. [30]

Also, recent studies [32,33] have shown that <0 0 1> oriented single crystals of the PMN-PT on the rhombohedral side of morphotropic phase boundary compositions exhibit extraordinarily large electromechanical coupling coefficients (>90%) and piezoelectric coefficients (d_{33}>2000 pC/N). Though according to the crystallographically, <1 1 1> is the polar direction, considerable domain reorientation under bias is known to take place for this orientation and materials tend to depole upon removal of the electric field. In contrast, the <0 0 1> direction is found to have a stable domain configuration, and excellent piezoelectric properties have been observed.

In this study, the raw <0 0 1> oriented PMN-0.30PT single crystals sample of a cylinder shape was made by ID saw, then cut by our wire saw machine to get wafers. As mentioned previously, only possible R–O and R–M phase transitions driven by wire saw

cutting down force were presumed, and then X-ray powder diffraction and Raman Spectra were measured for local and partial phase transformation analysis.

3.2 Experimental Methods

Under different cutting speed V_x combined with or no vibration assistance, several wafer samples of half circle shape were prepared, and the surfaces of these specimens were cleaned by Acetone. X-ray powder diffraction measurements were performed by using a high-resolution Siemens D5000 diffractometer with Cu *K*-alpha radiation confirmed the formation of phases with no evidence of any impurities. Copper tube was operated at $V = 45kV$ and $I = 30$ mA. The full diffraction patterns at the selected Bragg angle in the range of 15°-65° were recorded by using the scanning method with a step $\left|\Delta(2\theta) = 0.02^o\right|$ and a counting time of 10 seconds. Crystal structure refinements were performed using the profile Rietveld method.

The Raman spectra were collected using a T64000 Y von-Jobin multi-channel triple monochromator spectrometer (micro-Raman configuration, backscattering geometry). The 488 nm argon ion laser excitation line was used. Spot size of 20-30 micrometer, focus of 250 micrometer, objective of 20 times, wavenumber of 150-1000 cm^{-1} were set. For better local phase transition analysis, especially defining the different phases at the peak and valley locations, points scanning along the lines that are parallel or perpendicular to the surface waviness direction were delicately chosen and operated.

3.3 Results and Discussion

3.3.1 X-ray Results

Figure 3.3 presents the comparing of X-ray diffraction pattern of <0 0 1> oriented PMN-0.30PT single crystals sample cut by wire saw, ID saw and theoretical generated by GSAS software. The same machine information was input, theoretical modeling X-ray diffraction patterns of different phase composition were calculated by GSAS software. Compared with the theoretical X-ray fitting curve of multiply phases or single phase, detailed analysis of the peak broadening reveals the phases in wafer cut by wire saw under different cutting down speed and cut by ID saw are different. For example, around the Bragger angle range of 44-46°, this very clear and special area could be seen in Fig. 3.4, corresponding to the Rhombohedral and Orthorhombic two phases coexistence, there are three theoretical peaks very closed to each other, and for only single Orthorhombic phase there are only two peaks apart with each other, if compared with the experimental X-ray diffraction patterns of each case, it is very easy to find the peak shifts and broadening different between each case which means the phases composition different from each other. However, from this comparing, we still cannot define the ratio of phase composition in each case, and how the phase transition underwent, evenly in all direction or very inhomogeneous locally. It is very reasonable to explain the observed shift peak positions and different intensities since the lower-symmetry phases exist in this and related systems that of orthorhombic O and the ratio of this phase different in each case.

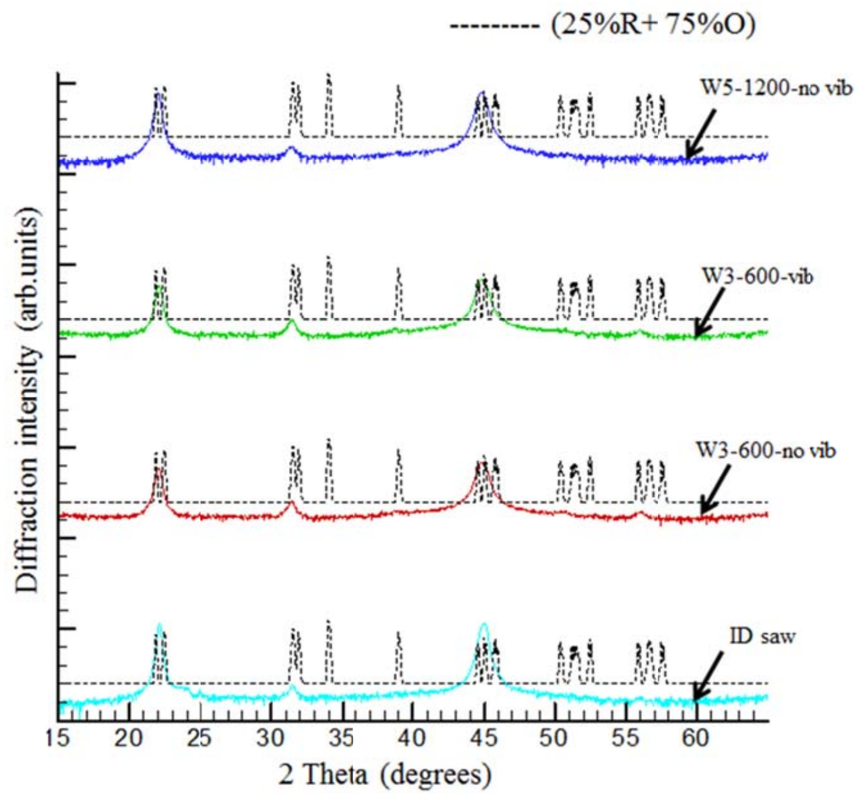
--------- (25%R+ 75%O)
W5-1200-no vib
W3-600-vib
W3-600-no vib
ID saw
Diffraction intensity (arb.units)
15
20
25
30
35
40
45
50
55
60
2 Theta (degrees)

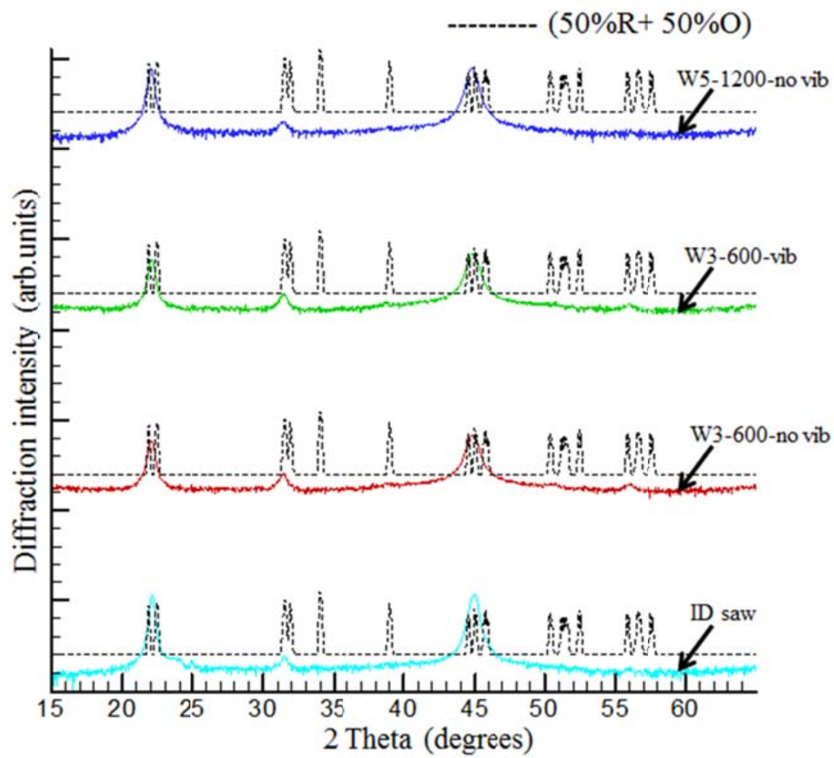
--------- (50%R+ 50%O)
W5-1200-no vib
W3-600-vib
W3-600-no vib
ID saw
Diffraction intensity (arb.units)
15
20
25
30
35
40
45
50
55
60
2 Theta (degrees)

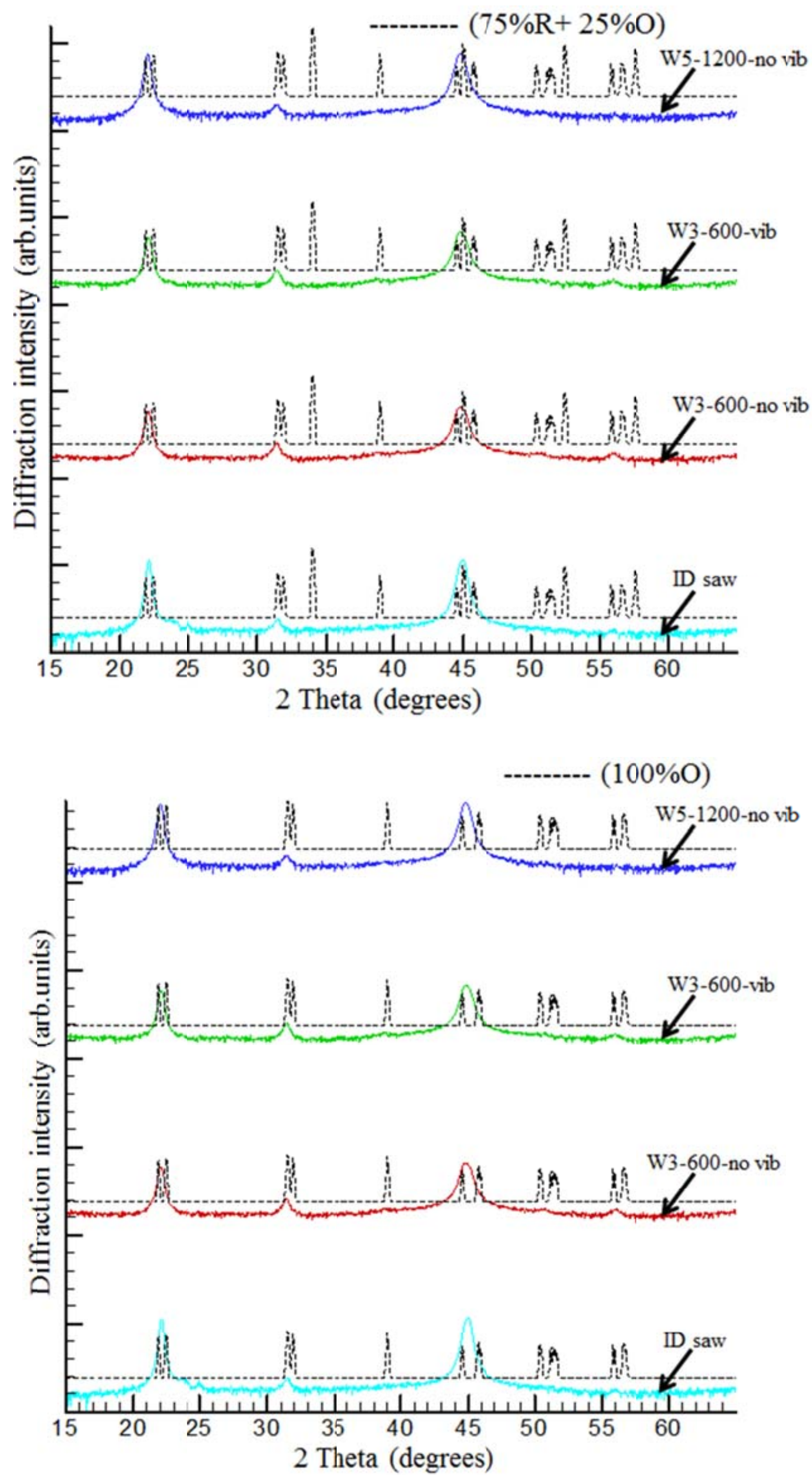

Fig. 3.3 X-ray diffraction pattern of <0 0 1> oriented PMN-0.30PT single crystals cut by wire saw, ID saw and theoretical

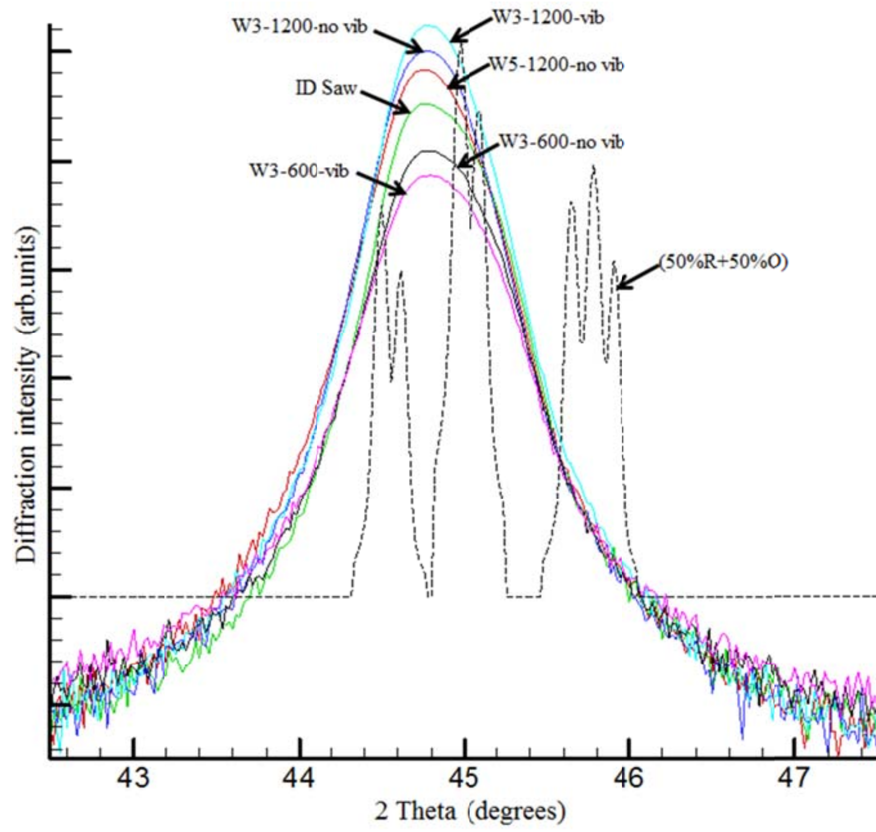
W3-1200-no vib
W3-1200-vib
W5-1200-no vib
ID Saw
W3-600-no vib
W3-600-vib
(50%R+50%O)
Diffraction intensity (arb.units)
43
44
45
46
47
2 Theta (degrees)

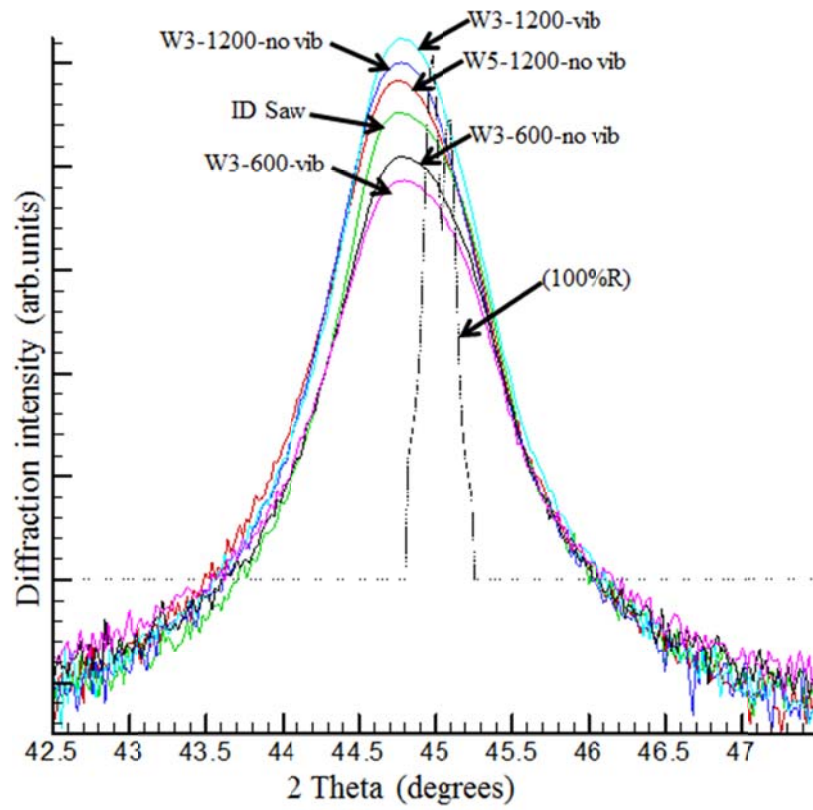
W3-1200-vib
W3-1200-no vib
W5-1200-no vib
ID Saw
W3-600-no vib
W3-600-vib
(100%R)
Diffraction intensity (arb.units)
42.5
43
43.5
44
44.5
45
45.5
46
46.5
47
2 Theta (degrees)

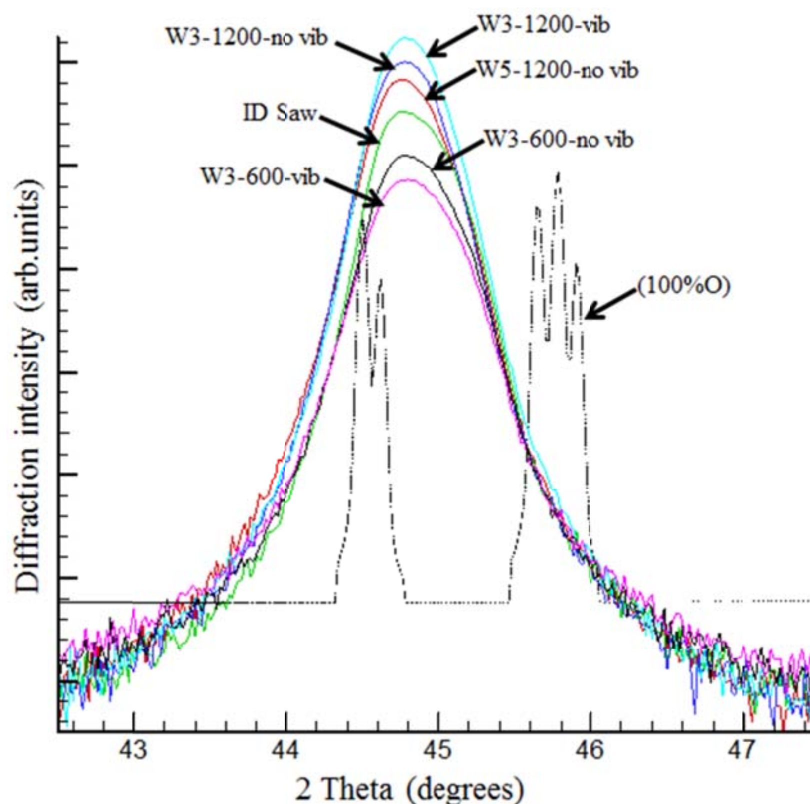

Fig. 3.4 Selected regions of the X-ray diffraction pattern of <0 0 1> oriented PMN-0.30PT single crystals cut by wire saw, ID saw and theoretical

3.3.2 Raman Scattering Results

The Raman spectra presented in Fig.3.5 is at different locations of the wafer surface that parallel and perpendicular to the waviness direction; consist of a number of broad lines. The PMN-PT Raman spectra can be divided into three characteristic regions of frequency: the low frequency region, which is approximately up to 150 cm^{-1}; the intermediate frequency region, which is approximately from 150 to 500 cm^{-1}; and the high frequency region, which is from 500 to 800 cm^{-1}. According to the attempts of mode assignment in the case of PMN[34] and especially due to lattice dynamics calculations performed by Prosandeev et al.[35], the low frequency region can be attributed to the Pb-BO_6 stretching modes. The

modes from the intermediate frequency region can be classified as mixed B-O-B bending and O-B-O stretching, while those from the high frequency region as B-O-B stretching.

The Raman spectra shown in Fig. 3.5 seem to be similar to each other; however, the qualitative analysis reveals noticeable changes in these Raman spectra at different locations. The most significant difference that can be seen in the frequency range of 500 to 650 cm^{-1}, as seen in Fig.3.6 and Fig. 3.7, at different locations of the wafer surface, some Raman modes become narrower and even new modes near 500 cm^{-1} appears, the frequencies and the line widths exhibit the characteristic jumps observed in this region. It is probable that these jumps can indicate the changes in the local symmetry between the rhombohedral(R3*m*), the monoclinic symmetry (P*m*), and the orthorhombic symmetry (P*mm*2). Moreover, as can be seen in Fig.3.6, which corresponds to different location cases that perpendicular to the waviness and apart of waviness width at 250 µm, characteristic jumps between each case can indicate the phases different along the direction perpendicular to waviness. However, as can be seen in Fig.3.7, which corresponds to different location cases that parallel to the waviness, no very obvious frequencies and line widths jumps could be found, which means along the direction that parallel to the waviness direction no much phase transitions occurred, the little difference and asymmetry could be possible explained by Lattice distortion or so, even if there is phase transition, at most very small partial transformations.

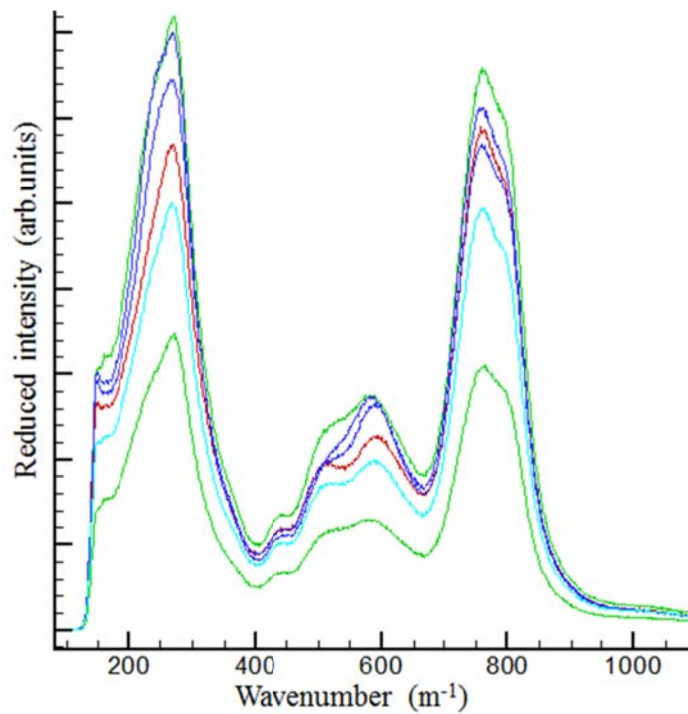

Fig. 3.5 Raman spectra of the <0 0 1> oriented PMN-0.30PT single crystal wafer at different locations that parallel and perpendicular to the waviness direction

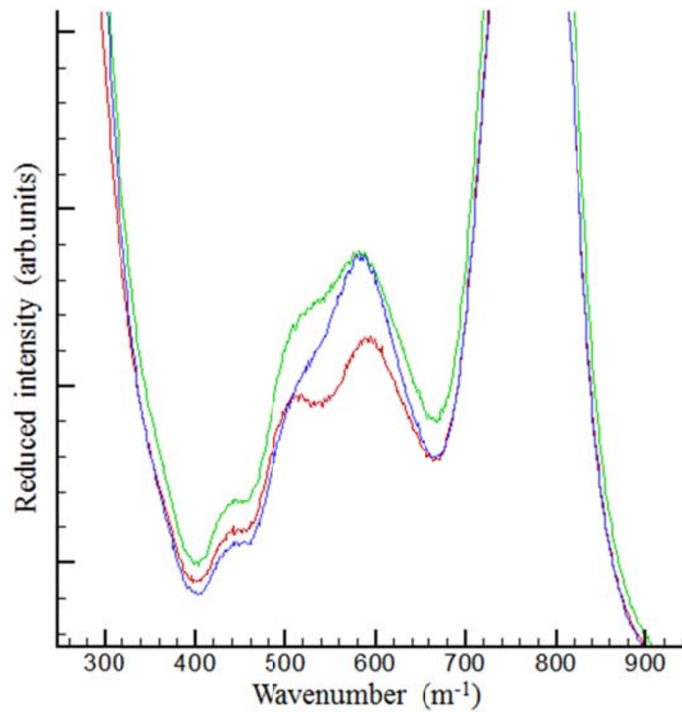

Fig. 3.6 Selected region of Raman spectra of the <0 0 1> oriented PMN-0.30PT single crystal wafer at different locations that perpendicular to the waviness direction

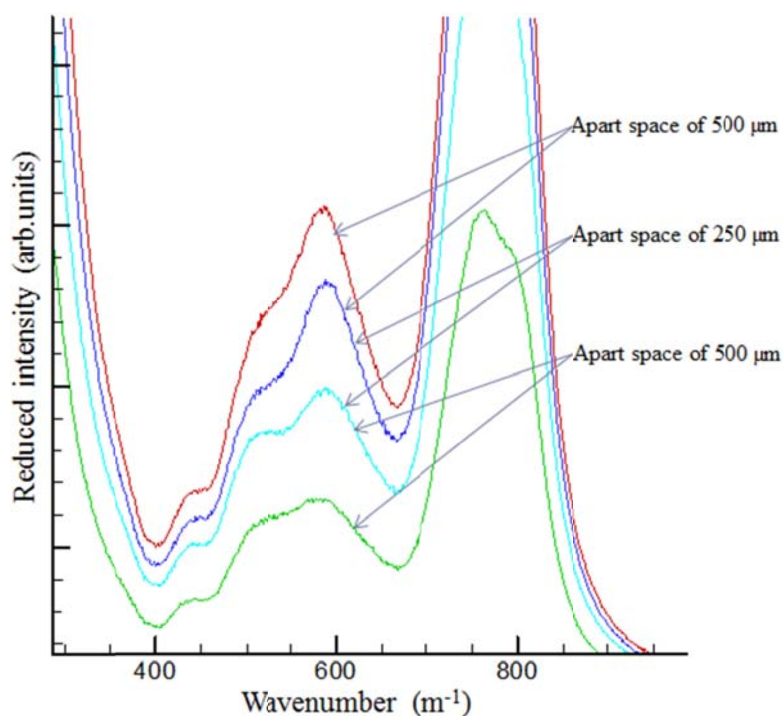

Fig. 3.7 Selected region of Raman spectra of the <0 0 1> oriented PMN-0.30PT single crystal wafer at different locations that parallel to the waviness direction

3.4 Conclusion

Phase transition was defined by comparing the experimental X-ray diffraction pattern of each case cut by wire saw or ID saw and the theoretical fitting curve under different phase composition, because the peak broadening and shift different in each case, it is obviously could be explained that the phase ratio in composition different in each case, especially the different ratio of lower-symmetry phase Orthorhombic. However, the detailed ratio of phase transition and how it underwent evenly or not cannot be defined in this analysis, further work needed to complete it.

CHAPTER 4 SUMMARY AND DISCUSSION

In this experimental study, the role of wire saw processing parameters on the final PMN-PT single crystals wafer surface roughness and waviness were investigated. Several analytical tools were utilized including SEM imaging of the subsurface damages; XRD and micro-Raman surface analysis to uncover the machining induced phase transformation. Based on the result of the parametric study, the following conclusion can be drawn.

1. Better surface quality can be generated if the force per cutting grit can be minimized. Such force is controlled by the ratio of the down feed to wire speed. Accordingly, any attempt to increase the down feed speed has to be accompanied by increase in the wire speed. Such attempt would be bounded by the wire stability and vibration.

2. Reduction of the down feed to the wire speed ratio at the same wire tension has showed improved Ra and RMS of the cut surface.

3. Better surface characteristics could be attained with vibration assistance wire saw cutting process, because of lateral crack initiated by intermittent unloading could prevent the vertical crack propagation and protect as a shield.

4. Phase transformation of PMN-PT single crystals can be also minimized by lowering the down feed to the wire speed ratio. However, exact reduction level needs further investigations.

BIBLIOGRAPHY

1. Kao, I., Prasad, V., Chiang, F. P., Bhagavat, M., Wei, S., Chandra, M., Costantini, M., Leyvraz, P., Talbott, J., and Gupta, K., 1998 "Modeling and experiments on wire saw for large silicon wafer manufacturing," The 8th Int. Symp. on Silicon Mat. Sci. and Tech., San Diego, May.
2. Buttner, A., 1985, "ID sawing-diameters increase," Ind. Diamond Rev., 45, pp. 77-79.
3. Struth, W. F., Steffens, K., and Konig, W., 1988, "Wafer slicing by internal diameter sawing," Precis. Eng., 10, pp. 29-34.
4. Fountain, C. W., and Peck, R. L., 1970, "Simple, inexpensive wire saw for small specimens," J. Phys. E, 3, pp. 725-726.
5. Anderson, J. R., 1980, "Wire saw for low damage, low kerf loss wafer," 14th IEEE Photovoltaic Specialists Conference, pp. 815-819, Phoenix, AZ.
6. Wells, R., 1987, "Wire saw slicing of large diameter crystals," Solid State Technology, Sept., pp. 63-65.
7. Kojima, M., Tomizawa, A., and Takase, J., 1990, "Development of new wafer slicing equipment," Sumitomo Kinzoku, 42, pp. 218-224.
8. Moller, J. H., "Basic Mechanisms and Models of Multi-Wire Sawing", Advanced Engineering Materials V.6 No.7 (2004) 501-513.
9. Li, J., Kao, I., and Prasad, V., 1998, "Modeling stresses of contacts in wire saw slicing of polycrystalline and crystalline ingots; Application to silicon wafer production," ASME J. Electron. Package, 120, No. 2, pp. 123-128, June.

10. Bhagavar, M., Prasad, V., and Kao, I., 2000, “Elasto-hydrodynamic interaction in the free abrasive wafer slicing using a wire saw: Modeling and finite element analysis,” ASME J. Tribol., 122, No. 2, pp. 394-404, Apr.

11. Clark, W.I., Shih, A.J., Hardin, C.W., Lemaster, R.L., McSpadden, S.B., “Fixed abrasive diamond wire machining-Part I: process monitoring and wire tension force”, International Journal of Machine Tools and Manufacture V.43 (2003a) 523-532.

12. Clark, W.I., Shih, A.J., Hardin, C.W., Lemaster, R.L., McSpadden, S.B., “Fixed abrasive diamond wire machining-Part Π: experiment design and results”, International Journal of Machine Tools and Manufacture V.43 (2003b) 533-542.

13. Bhagavat M., Kao I., “Computational Model for Free Abrasive Machining of Brittle Silicon Using a Wire Saw”, Electronics Manufacturing Issues ASME, DE-Vol. 104, (1999) pp21-30.

14. Jaffe, B., W.R. Cook, and H. Jaffe, Piezoelctric Ceramics 1971, London: New York, Academic Press.

15. Noheda, B., D.E. Cox, G. Shirane, Z.-G. Ye, and J. Gao, Phase diagram of the ferroelectric relaxor $(1-x)[Pb(Mg_{1/3}Nb_{2/3})O_3]-xPbTiO_3$. Phys. Rev. B: Condens. Matter, 2002. 66: p. 054104-1-10.

16. Singh, A.K. and D. Pandey, Structure and the location of the morphotropic phase boundary region in $(1-x)[Pb(Mg_{1/3}Nb_{2/3})O_3]-xPbTiO_3$. J. Phys. Rev. B: Condens. Matter, 2001. 13(48): p. 931-936.

17. Ye, Z.G., Crystal chemistry and domain structure of relaxor piezocrystals. Curr. Opin. Solid State Mater. Sci., 2002. 6(1): p. 35-44.

18. Singh, A.K. and D. Pandey, Evidence for M_B and M_C phases in the morphotropic phase boundary region of (1-x)[Pb($Mg_{1/3}Nb_{2/3}$)O_3]-$x$$PbTiO_3$: A Rietveld study Phys. Rev. B: Condens. Matter, 2003. 67(6): p. 064102.

19. A.G. Evans, D.B. Marshall, Wear mechanisms in Ceramics, Fundamentals of Friction and Wear of Materials, ASM Materials Science Seminar, Pennsylvania,1980, pp.439-449.

20. G. Fu, A. Chandra, S. Guha, G. Subhash, A plasticity based model of material removal in chemical-mechanical polishing (CMP), IEEE Transactions on Semiconductor Manufacturing, 14 (4) (2001) 406-417.

21. B.R. Lawn, A.G. Evans, D.B. Marshall, Elastic/plastic indentation damage in ceramics: the median/radial crack system, Journal of the American Ceramic Society, 63 (9-10) (1980) pp.574-581.

22. Singh AK, Pandey D. Structure and the location of the morphotropic phase boundary region in (1-x)[Pb($Mg_{1/3}Nb_{2/3}$)O_3]-$x$$PbTiO_3$. J Phys Condens Mat 2001; 13:931.

23. B. Noheda, D. E. Cox, G. Shirane, Z. G. Ye, and J. Gao. Phase diagram of the ferroelectric relaxor (1-x)[Pb($Mg_{1/3}Nb_{2/3}$)O_3]-$x$$PbTiO_3$. Phys. Rev. B 66, 054104 (2002).

24. Ye ZG. Crystal chemistry and domain structure of relaxor piezoe-crystals. Curr Opin Solid State Mater Sci 2002; 6: 35.

25. Singh AK, Pandey D. Evidence for M_B and M_C phases in the morphotropic phase boundary region of (1-x)[Pb($Mg_{1/3}Nb_{2/3}$)O_3]-$x$$PbTiO_3$ single crystals with different orientations. J Phys Condens Mater 2003; 15: 6899.

26. Viehland D, Li JF. Anhysteretic field-induced rhombohedral to orthorhombic transformation in <1 1 0>-oriented 0.7[$Pb(Mg_{1/3}Nb_{2/3})O_3$]-0.3$PbTiO_3$ crystals. J Appl Phys 2002; 92: 7690.

27. Mclaughlin EA, Liu T, Lynch CS. Relaxor ferroelectric PMN-32%PT crystals under stress and electric field loading: I-32 mode measurements. Acta Mater 2004; 52: 3849.

28. A. Slodczyk, P. Daniel, A. Kania. Local phenonmena of (1-x)[$Pb(Mg_{1/3}Nb_{2/3})O_3$]-$x$$PbTiO_3$ single crystals ($0 \leq x \leq 0.38$) studied by Raman scattering. Phys Rev B 2008; 77: 184114.

29. McLaughlin EA, Liu T, Lynch CS. Relaxor ferroelectric PMN-32%PT crystals under stress, electric field and temperature loading: II-33-mode measurements. Acta Mater 2005; 53: 4001.

30. K.G. Webber, R. Zuo, C S. Lynch. Ceramic and single-crystal (1- x) PMN- x PT constitutive behavior under combined stress and electric field loading. Acta Mater 2008; 56: 1219-1227.

31. Zhao X, Wang J, Luo H, Chan HLW, Choy CL. Effect of a bias field on the dielectric properties of 0.69[$Pb(Mg_{1/3}Nb_{2/3})O_3$]-0.31$PbTiO_3$ single crystals with different orientations. J Phys Condens Mater 2003; 15: 6899.

32. Park, S.E., Shrout, T. R.: Ultrahigh strain and piezoelectric behavior in relaxor based ferroelectric single crystals. J. Appl. Phys. 82(4), 1804-1811(1997).

33. Uchino, K.: High electromechanical coupling piezoelectrics: relaxor and normal ferroelectric solid solutions. Solid State Ionics 108(1-4), 43-52(1998).

34. E. Husson, L. Abello, and A. Morell, Mater. Res. Bull. 25,539(1990).

35. S. A. Prosandeev et al. Phys. Rev. B 70, 134110(2004).

ACKNOWLEDGEMENTS

I would like to take this opportunity to express my thanks to those who helped me with various aspects of conducting research and the writing of this thesis, first and foremost, Dr. Ashraf F. Bastawros for his guidance, patience and support throughout this research and the writing of this thesis. His insights and words of encouragement have often inspired me and renewed my hopes for completing my graduate education. I would also like to thank my committee members for their efforts and contributions to this work: Dr. Thomas J. Rudolphi and Dr. Wei Hong.